On the application of scattering matrix measurements to detection and identification of major types of airborne aerosol particles: Volcanic ash, desert dust and pollen

Juan Carlos Gómez Martín [a],*, Daniel Guirado [a], Elisa Frattin [b], Maria Bermudez-Edo [c], Paloma Cariñanos Gonzalez [d,e], Francisco José Olmo Reyes [e,f], Timo Nousiainen [g], Pedro J. Gutiérrez [a], Fernando Moreno [a], Olga Muñoz [a],*

[a] Instituto de Astrofísica de Andalucía (IAA-CSIC), 18008, Granada, Spain
[b] Department of physics and Astronomy "Galileo Galilei", University of Padova, Padova, Italy
[c] Departamento de Lenguajes y Sistemas Informáticos, Escuela Técnica Superior de Ingenierías Informática y de Telecomunicación, Universidad de Granada, Granada, Spain
[d] Departamento de Botánica, Facultad de Farmacia, Universidad de Granada, 18071, Granada, Spain
[e] IISTA-CEAMA, Andalusian Institute for Earth System Research, Universidad de Granada, 18071, Granada, Spain
[f] Departamento de Física Aplicada, Facultad de Ciencias, Universidad de Granada, 18071, Granada, Spain
[g] Finnish Meteorological Institute, FI-00560, Helsinki, Finland

ARTICLE INFO

ABSTRACT

Atmospheric aerosols play key roles in climate and have important impacts on human activities and health. Hence, much effort is directed towards developing methods of improved detection and discrimination of different types of aerosols. Among these, light scattering-based detection of aerosol offers several advantages including applications in both in situ and remote sensing devices. In this work, new scattering matrix measurements for two samples of airborne desert dust collected in Spain and China are reported. The average extrapolated scattering matrices of airborne desert dust and of volcanic ash at two wavelengths have been calculated and compared with the aim of finding criteria to distinguish these two types of aerosol. Additionally, the scattering matrix of cypress pollen has been measured and extrapolated to explore differences with mineral dust that can be exploited in atmospheric detection. Field measurements of the backscattering linear depolarization ratio $\delta_L(180°)$ are used to obtain information about non-sphericity and discrimination between fine and coarse aerosol. However, the average $\delta_L(180°)$ for the three types of aerosols considered in this work in the visible spectral range is $\delta_L(180°) = 0.40 \pm 0.05$. This shows that $\delta_L(180°)$ is not informative about the composition or morphology of irregular particles. By contrast, measurements of scattering matrix elements or depolarization ratios at different scattering angles may provide information about the structural differences of particles, and in particular may enable to differentiate airborne volcanic ash from desert dust, which are otherwise similar in terms of size and optical constants. Cypress pollen shows a characteristic degree of linear polarization curve that is very different from that of polydisperse irregular mineral dust. Light scattering field instruments and remote sensing methods could extract more information about the characteristics of aerosol particles if modifications were introduced to measure the phase curves of several scattering matrix elements or depolarization ratios.

1. Introduction

Mineral particles constitute a large fraction of primary atmospheric aerosol and they are known to affect climate directly by changing the Earth's radiation budget and indirectly by modifying cloud properties [1]. They are also thought to modify the global carbon cycle through iron fertilization of the ocean surface [2] and by supplying nutrients to land vegetation on nutrient-deficient soil [3]. The mean diameters of mineral aerosols vary roughly between 0.02 μm and 100 μm. Desert regions are the main source of primary mineral aerosols, which can be blown thousands of

kilometers away from their origin. The Sahara Desert dust spreads across the Mediterranean basin and Europe, but it also reaches the Caribbean Sea, and North, Central and South America [4], where it contributes to the nutrient inflow to the Amazon rainforest [3]. The Gobi Desert dust affects eastern Asia and can reach as far as western North America [5]. The Fifth Assessment Report of the Intergovernmental Panel on Climate Change (IPCC) in 2013 estimated the global source strength of for mineral dust between 1000 and 4000 Tg yr^{-1} [1].

Volcanic eruptions are an important source of primary and secondary aerosol. Explosive volcanic eruptions with volcanic explosivity index (VEI) higher than 4 inject gases and solid aerosol particles into the stratosphere, which may remain there from months to several years, changing its composition. Secondary sulfate aerosols are generated by transformation of gas-phase SO_2 injected into the stratosphere into condensable H_2SO_4, while primary volcanic aerosols are silicate ashes ejected at the time of the explosion. Stratospheric sulphate aerosol plays a major role in the atmospheric radiative budget, and the climate impacts of explosive volcanic eruptions may last for years. Volcanic ash particles may remain for months in the stratosphere and are believed to influence sulphate aerosol formation [6]. The total emissions of volcanic ash into the troposphere by smaller volcanic eruptions (VEI $\leq$ 4), which are the most frequent, are estimated to be 20   Tg yr^{-1} [7], i.e. two orders of magnitude lower than the source strength of soil mineral dust. However, another important aspect of the presence of volcanic ash clouds in the mid- and upper troposphere is the danger that they pose to aviation [8].

Primary biological aerosol particles (PBAP) encompass bacteria and archaea, fungal spores, pollen, viruses, algae and cyanobacteria, lichens and others [9]. Estimated PBAP source strengths are in the range between 50 and 1000 Tg yr^{-1} [1]. It has been suggested that they influence clouds and precipitation, and thus they may have an impact on the hydrological cycle and climate, at least on regional scales [10–12]. Moreover, PBAP are linked to a range of adverse health effects. Airborne pollen, for example, is one of the most common triggers of seasonal allergies. It affects over 24% of European population with children quota up to 40% [13]. Pollinosis is specially acute in urban environments, due to a binding of urban pollutants with allergenic proteins [14]. Episodes of concurrent airborne pollen peaks and desert dust intrusions are frequent in the Mediterranean basin, East Asia and elsewhere [15,16].

In order to study the radiative impact of airborne particles, properties such as the phase (scattering) function need to be known. Satellite radiometers, for example, measure the intensity (radiance) of reflected light at different wavelengths and, in some cases, at several scattering angles. These have been key to image, for example, the transport of Saharan aerosol to the Amazonian basin [4]. Remote sensing measurements of scattered sunlight or upwelling infrared radiance made by orbiting satellites are also highly useful for mapping the positions of volcanic ash clouds to provide a warning system for aviation, and for improving cloud trajectory models by providing frequently updated information on the mass estimates and the position of the clouds of volcanic ashes [8]. The ground-based sun-sky scanning radiometer network AERONET [17–19] provides global near real-time observations of aerosol spectral optical thickness and angular distribution of sky radiances as well as derived parameters such as particle size distributions [20,21].

The retrieval of aerosol characteristics can be significantly improved when the polarization of the reflected light is measured simultaneously with the phase function. Different aerosol types have different polarization signatures, and therefore polarimetry holds the potential to distinguish between different components of the aerosol load. Multi-angular and multi-spectral polarimetric measurements have been performed with a number of remote

sensing instruments such as the POLDER series [22]. Ground-based and aircraft- and satellite-borne depolarization lidars [3,22–30] use additional optical receiver components (a polarization beam splitter and a second photodetector) to perform measurements of the depolarization ratio, i.e., the ratio of the backscattered power in the planes of the polarization orthogonal and parallel to that of the linearly polarized source. This ratio depends on the scattering matrix elements of the scatterers and can be used to infer the microphysical properties of aerosol, clouds and precipitation.

Regarding pollen, one of the major challenges is developing low-cost in situ and remote detection devices for public health monitoring, crop pollination monitoring, and research on the natural migration of organisms and biodiversity [31]. In some situations, there is a need for specific taxonomic pollen identification, while in other cases only general information is required. In situ detection of mineral aerosol and bioaerosol includes trapping and counting [32,33], microelectromechanical detection [34,35], fluorescence spectroscopy [36] and Raman spectroscopy [13,37,38], as well as light scattering in different configurations. Some multi-instrumented detectors combine several of the aforementioned techniques [39–48] and may implement machine learning techniques to discriminate between different kinds of aerosol and pollen taxa [45,48]. Trapping and counting remains the field golden standard, but this method is not only time consuming, but also prone to calibration errors [49], despite automation using image recognition techniques to infer the different pollen taxa and their quantities [50,51]. Detection of light scattered by particles usually involves measuring forward scattering and forward/side scattering ratios to infer some morphological features of the particles, such as size, shape and surface structure [52,53]. Diffraction imaging/holography techniques [54], which allow imaging of single pollen grains, have been implemented in state-of-the art devices [48,55]. Measurements of the degree of linear polarization of the light scattered by pollen grains has also been implemented in a limited number of instruments [48,56]. Remote sensing of bioaerosol is performed using fluorescence [57] and depolarization lidars [58].

The advantages of light scattering-based detection of aerosol include application to both in situ detection and remote sensing, bulk detection, use of several estimators from different elements of the scattering matrix, multi-angle and multi-wavelength measurements and potential for building a range of cheap instruments, including hand held instruments. However, accurate retrieval of aerosol characteristics is usually hampered by the lack of information on the scattering properties of realistically shaped aerosols. This holds in particular for their phase function and angular distribution of the polarization of singly scattered light for incident unpolarized light. Thus, laboratory measurements of the scattering matrix of representative dust samples under controlled conditions are important for interpreting field observations [59,60]. Furthermore, commonly used techniques such as lidar backscattering measurements still require further development to enable discrimination between different types of aerosol [61].

The objective of this work is to explore ways of improving the detection and identification of different types of atmospheric aerosol using satellite or ground-based remote sensing of scattered light and in situ devices equipped with light scattering units. We look for specific light scattering characteristics of natural airborne aerosol beyond the backscattering depolarization ratio that can be used to detect and classify particles such as mineral dust and pollen grains, with different composition and size and shape distributions. For this purpose, we have reviewed scattering matrix measurements of volcanic ash samples compiled at the Granada-Amsterdam Light Scattering Database [60] and we have carried out new measurements of the scattering matrix of long-range airborne desert dust samples and a common pollen sample in the

Cosmic Dust Laboratory (CODULAB) at IAA-CSIC [59,62]. We have used hierarchical clustering analysis to investigate relationships between the scattering matrices of the samples considered in this work and those included in the Granada-Amsterdam Light Scattering Database. Based on our findings, we suggest possible target observables for monitoring devices that may enable enhanced aerosol measurements.

2. Methodology

2.1. Experimental set-up

Detailed descriptions of the CODULAB apparatus at IAA-CSIC and its antecessor set-up at the Free University of Amsterdam have been reported elsewhere [59]. All published results are available at the Granada-Amsterdam Light Scattering Database (www.iaa.es/scattering) [60]. Briefly, a laser beam in the visible spectral range generated with a HeCd laser (441.6 nm), a HeNe laser (632.8 nm), a tunable Argon–Krypton laser source (Melles Griot 35 KAP 43, laser wavelengths 448 nm and 647 nm in this work) or more recently with diode lasers (Coherent OBIS LX FP, 514 nm in this work), passes through an integrated polarizer and an electro-optic modulator. The beam is subsequently dispersed by an aerosol cloud [62] and the scattered light is collected at different angles by a photomultiplier mounted on a goniometer ring. Due to experimental constraints, measurements cannot be carried out in the whole scattering angle range ($0° \leq \theta \leq 180°$), but typically from $3°$ to $177°$. Two additional optical elements (a quarter-wave plate and an analyzer), are optionally placed in the detector photomultiplier. The application of an oscillating voltage to the modulator combined with lock-in amplified detection allows the determination of all the elements of the scattering matrix of the aerosol sample [63] by using five different configurations of the optical elements. Each configuration requires typically one load of the reservoir of the aerosol generator.

2.2. Scattering matrix and depolarization ratios

Assuming mirror symmetry and randomly oriented particles in the sample [64], the 4×4 scattering matrix has six non-zero independent real elements:

$$\mathbf{F} = \begin{pmatrix} F_{11} & F_{12} & 0 & 0 \\ F_{12} & F_{22} & 0 & 0 \\ 0 & 0 & F_{33} & F_{34} \\ 0 & 0 & -F_{34} & F_{44} \end{pmatrix} \tag{1}$$

The scattering matrix elements F_{ij} depend on wavelength λ and scattering angle θ, and these dependences are governed by particle size, morphology and complex refractive index. The $F_{ij}(\theta)$ curves measured at CODULAB are normalized to $F_{11}(\theta)$. The element $F_{11}(\theta)$ itself (i.e. the phase function) is reported normalized to unity at $\theta = 30°$. The degree of linear polarization (DLP) for unpolarized incident light is given by DLP = $-F_{12}(\theta)/F_{11}(\theta)$.

The linear depolarization ratio δ_L of an ensemble of randomly oriented particles is given by:

$$\delta_L = \frac{1 - F_{22}/F_{11}}{1 + 2F_{12}/F_{11} + F_{22}/F_{11}} \tag{2}$$

where F_{11}, F_{12} and F_{22} are elements of the scattering matrix.

Note that in the backscattering direction $F_{12}(180°) = 0$ [65]. The backscattering linear depolarization ratio $\delta_L(180°)$ is an indicator of particle nonsphericity, although it shows a complex dependence on particle size and refractive index [66]. Lidar measurements of $\delta_L(180°)$ provide a way of discriminating fine-mode from coarse-mode aerosol [61].

For a collection of randomly oriented particles with mirror symmetry, the circular depolarization ratio is given by:

$$\delta_C = \frac{1 + F_{44}/F_{11}}{1 - F_{44}/F_{11}} \tag{3}$$

where F_{11} and F_{44} are elements of the scattering matrix. The backscatter circular depolarization ratio $\delta_C(180°)$ is another parameter that can be measured by lidar to investigate whether the mirror symmetry condition is fulfilled [61,66].

The scattering matrix is currently measured at CODULAB in the $3° \leq \theta \leq 177°$ range, but must be known for $0° \leq \theta \leq 180°$ for radiative transfer modeling purposes [67] and other applications including the determination of reference backscattering depolarization ratios $\delta_L(180°)$ for lidar studies. For this reason, an extrapolation technique for the phase curves of the non-zero elements of the scattering matrix in Eq. (1) is required. An earlier version of this technique was described by Escobar-Cerezo et al. [68]. In this work we use an improved version, which takes advantage of symmetry in the scattering plane to add an additional datapoint so that $F_{11}(\theta)$ and $-F_{12}(\theta)/F_{11}(\theta)$ are interpolated in the backscattering direction between $177°$ and $183°$. In this way, the calculation of the matrix elements at the backscattering direction is better constrained than if a simple extrapolation towards $180°$ is performed. First, the $F_{11}(\theta)$ forward peak ($0°$ to $3°$) is obtained from Mie theory by considering a cloud of spheres with the same refractive index and size distribution than the actual sample. This is because, in the forward direction, the phase function does not depend on the shape of the particles [69]. Moreover, the effect of the shape has been checked to be negligible in the range of a few degrees from $0°$ for some simple shapes [70]. The measurements, which have an arbitrary scaling, are rescaled to achieve continuity with the Mie calculated forward peak. In a second step, $F_{11}(\theta)$ is extrapolated in the backward direction, based on its symmetry in the two halves of the scattering plane for randomly oriented particles. For this purpose, a symmetric function G_{11} is defined as follows:

$$G_{11}(\theta) = \begin{cases} F_{11}(\theta); & 0 \leq \theta < \pi \\ F_{11}(2\pi - \theta); & \pi \leq \theta < 2\pi \end{cases} \tag{4}$$

This function has a gap of a few unknown points in the middle, which are obtained by interpolation using a cubic splines method to retrieve $F_{11}(\theta)$ in the full angular range. Once the phase function has been extrapolated forward and backward, it is re-normalized according to energy conservation [65]:

$$\frac{1}{2} \int_0^\pi \sin(\theta) F_{11}(\theta) \, d\theta = 1 \tag{5}$$

The $-F_{12}(\theta)/F_{11}(\theta)$ element must be zero at $\theta = 0$ and $\theta = 180°$ [63]. Moreover, the derivatives of all elements must be zero at the exact forward and backward directions [71]. Taking these constraints into account, a new function G_{12} is defined akin to Eq. (4), and the cubic splines interpolation method is again applied to fill the gap and retrieve the missing points in the backward direction. For retrieving the missing points of $-F_{12}(\theta)/F_{11}(\theta)$ in the forward direction, a new function H_{12} is defined:

$$H_{12}(\theta) = \begin{cases} -F_{12}(-\theta)/F_{11}(-\theta); & -\pi \leq \theta < 0 \\ -F_{12}(\theta)/F_{11}(\theta); & 0 \leq \theta < \pi \end{cases} \tag{6}$$

The gaps in H_{12} are filled by using again the cubic splines interpolation method. For the rest of the non-zero elements, we use the same method as for $-F_{12}(\theta)/F_{11}(\theta)$, considering null derivatives at $\theta = 0°$ and $\theta = 180°$ and the following conditions at exact forward and backward scattering: $F_{33}(0°)/F_{11}(0°) = F_{22}(0°)/F_{11}(0°)$, $F_{34}(0°)/F_{11}(0°) = 0$, $F_{44}(0°)/F_{11}(0°) = 2F_{22}(0°)/F_{11}(0°) - 1$, $F_{33}(180°)/F_{11}(180°) = -F_{22}(180°)/F_{11}(180°)$, $F_{33}(180°)/F_{11}(180°) = 0$ and $F_{44}(180°)/F_{11}(180°) = 1 - 2F_{22}(180°)/F_{11}(180°)$ [64,72].

Table 1
Summary of samples considered in this study.

Sample	Origin	Collection point	Processing
Chichon (Mexico)	Mar-Apr 1982 eruption	few km away within 24 h	
Lokon (Indonesia)	1996 eruption	few km away within 24 h	
Pinatubo (Philippines)	Jun 1991 eruption	few km away	crushing of larger debris
Redoubt (USA)	1989–1990 eruption	A:110 km away B:200 km away	coarse fraction removed by sieving
Spurr (USA)	Aug–Sep 1992 eruption	Ashton:270 km SE Anchorage:130 km E Gunsight: 265 km E Stop 33: 185 km E	
Mt. St. Helens (USA)	May 1980 eruption	6 km north of the crater	
Puyehue (Chile)	Jun 2011 eruption	150 km away from the source	
Eyjafjallajökull (Iceland)[a]	Apr 2010 eruption	5 km away from the source	
Sahara Desert dust*	Dust intrusion 2004	OSN Granada, Spain	
Gobi Desert dust*	Dust storm 2006	Beijing, China	
Cypress Pollen*	Pollination Feb 2020	Federico García Lorca Park, Granada, Spain	collected from pollen sacks; debris removed by sieving

[a] Scattering matrix measurements at blue wavelengths have not been previously reported. * New samples.

2.3. Selection of samples

Table 1 lists the samples of volcanic ash, desert dust and pollen considered in this study. Desert dust is an important reference atmospheric aerosol because it is very common and has a long atmospheric residence time. Saharan and Gobi Desert dust were retrieved very far away from their sources. The OSN sample was collected at the Observatory of Sierra Nevada (OSN) during a Sahara dust intrusion event in 2004. OSN is located 2896 m above sea level in the Sierra Nevada Mountain Range (Granada, Spain), more than 1500 km away from the dust source. For dust collection, a dedicated device was installed at the roof of the observatory at the beginning of the dust rainstorm. The sample was subsequently dried up and stored at CODULAB. The Gobi Desert sample was collected in Beijing directly from the tops of cars during a severe dust storm in 2006. In this paper we report measurements of the scattering matrices of these samples at 647 nm (both samples) and 488 nm (complete for the Gobi-Beijing sample, and only three elements for the Sahara-OSN sample, due to the small amount of dust collected, which was not enough to perform measurements for the remaining three elements).

Measurements of the scattering matrices at 441.6 nm and 632.8 nm of a number of volcanic ash samples have been published elsewhere [73–75]. Volcanic ashes present very similar scattering characteristics independent of the distance of the collection point to the source, type of volcanic explosion, etc., and therefore an average at 632.8 nm scattering matrix for 9 samples has been previously reported [75]. More recent measurements of volcanic ash matrices (Eyjafjallajökull and Puyehue samples) were carried out at 647 nm [76]. Measurements for Eyjafjallajökull at 488 nm are reported here for the first time.

For this study, we have collected a sample of cypress pollen, which is one of the predominant types of pollen in the city of Granada, Spain (37.18817N, 3.60667W), where CODULAB is located. Cypress is a common name for various coniferous trees belonging to the family Cupressaceae. The number of these trees in Granada is about 6000, i.e. about 15% of the trees within the city boundaries [78]. Because of the large number of cypresses and their high pollen production rate, Granada presents the second highest levels of pollen in Spain. Since 1992, the Unit of Aerobiological Sampling of the University of the University of Granada (UMA-UGr) has registered an average annual total value of 18081 cypress pollen grains per day and cubic meter in the urban atmosphere, representing 31% of the total, and only behind Olive pollen, which amounts to 36 % of the total. A clinical study in Granada has shown that ~30% of the population with pollinosis are sensitive to Cupressaceae pollen [79,80]. To obtain a pollen sample with the highest possible purity, cone-bearing branches with pollen sacks were collected from trees in the period immediately prior to flowering. Subsequently, the material was transferred to the laboratory to finish its maturation so that the opening of the sack would permit the release of pollen. The sample was then sieved to eliminate vegetal debris.

2.4. Sample characterization

2.4.1. Refractive index

The estimated complex refractive indices of the volcanic ash samples (Table 2) are discussed in previous publications [74–76]. For desert dust we consider the estimate by Volten et al. [73]. The real part of the refractive index of cypress pollen can be estimated to be in the range 1.3–1.54, while the imaginary part is close to zero [81,82].

2.4.2. Size distribution

The particle size distributions (PSDs) of the Chichon, Lokon, Pinatubo, Redoubt, Spurr and Mt. St. Helens samples were measured with a Fritsch particle sizer using the Fraunhofer approximation and have been reported elsewhere [74,75]. The Mt. St. Helens, Puyehue and Eyjafjallajökull volcanic ash samples were sized by laser light scattering (LLS) measurements with a Malvern Mastersizer 2000 using both the Fraunhofer approximation and the Lorenz-Mie theory, and the PSDs are also available from a previous publication [76]. The PSDs of the Sahara-OSN and Gobi-Beijing desert dust samples have been determined in this work with a Mastersizer 2000 apparatus, which uses water as dispersive medium. Table 2 lists the effective radii (r_{eff}) and variances (v_{eff}) of these PSDs as defined by Hansen and Travis [77]. Comparison of the r_{eff} and v_{eff} values of different samples gives some idea about the differences between their respective PSDs in terms of projected surface. For spheres, different PSDs with similar values of r_{eff} and v_{eff} are expected to produce similar scattering results for the same refractive index [77], and this should hold also for other geometries assuming that the shapes are sufficiently similar. A caveat to this metric is that for some older samples, only Fraunhofer PSDs are available, which leads to underestimation of r_{eff} and overestimation of v_{eff} as a result of a spurious enhancement in the submicron range [83] (see Mie and Fraunhofer r_{eff} and v_{eff} values in Table 2). Thus, it is convenient to determine both Fraunhofer and Mie PSDs for new samples in order to enable comparison with

Table 2
Complex refractive indices ($m = n - ik$) and size parameters (effective radii r_{eff} and variances v_{eff}, and power law index p) of the samples.

Sample	n	k	r_{eff}/μm [a]	v_{eff}	p [b]	λ/nm [c]
Lokon	1.5–1.6	10^{-5}–10^{-3}	7.1	2.6	3.01 ± 0.10	632.8, 441.6
Pinatubo	1.5–1.6	10^{-5}–10^{-3}	3.0	12.3	3.89 ± 0.02	632.8, 441.6
Redoubt A	1.48–1.56	1.8×10^{-3}	4.1	9.7	3.66 ± 0.03	632.8
Redoubt B			6.4	7.6	3.55 ± 0.03	632.8
Spurr Anchorage	1.48–1.56	2×10^{-2} -1.8×10^{-3}	4.8	8.8	3.58 ± 0.04	632.8
Spurr Ashton			2.7	4.9	3.80 ± 0.05	632.8
Spurr Gunsight			3.5	8.2	3.78 ± 0.06	632.8
Spurr Stop 33			14.4	6.6	3.74 ± 0.05	632.8
Mt. St. Helens	1.48–1.56	1.8×10^{-3}	4.1 (8.9)	9.5 (4.0)	3.72 ± 0.02	632.8
Chichon	1.5–1.6	10^{-3}	3.2	5.4	3.77 ± 0.05	632.8
Puyehue	1.48	2.7×10^{-4}	5.0 (8.6)	4.4 (2.2)	3.67 ± 0.04	647
Eyjafjallajökull	1.43–1.59	0-4×10^{-3}	4.0 (7.8)	5.9 (2.9)	3.59 ± 0.03	647, 488 [d]
Sahara-OSN	1.5--1.7	10^{-5}–10^{-3}	2.5 (4.0)	2.5 (1.8)	4.44 ± 0.11	647 [d], 488 [d]
Gobi-Beijing	1.5–1.7	10^{-5} --10^{-3}	4.6 (7.6)	2.9 (1.6)	3.70 ± 0.10	647 [d], 488 [d]
Cypress Pollen	1.3–1.54	~0	11.4	5×10^{-3}	n/a	514 [d]

[a] From laser light scattering particle sizing, using the Fraunhofer approximation. Numbers between brackets: using Mie theory. The effective variance is defined relative to the squared effective radius, which makes it dimensionless [77].
[b] Power law ($n_s(r) \propto r^{-p}$) exponent of the PSD in the 1 μm < r < 70 μm range. [c] Wavelength of the scattering matrix measurements. [d] This work.

older measurements. Moreover, r_{eff} and v_{eff} may be biased towards higher or lower values due to the presence of multiple modes in the PSD. An additional metric of the similarities between PSDs is the power law exponent p of the number PSD $n_s(r)$ (Table 2), i.e. the slope of the log $n_s(r)$ versus log r plot in a relevant size interval (i.e. sizes that contribute most to the scattering matrix in the experimentally accessible angular range).

Fig. 1a compares $n_s(r)$ for the Puyehue and Eyjafjallajökull volcanic ash samples, and for the new Sahara-OSN and Gobi-Beijing desert dust samples. Mie and Fraunhofer PSDs are essentially the same for $r > 1.2$ μm. In the submicron range, Fraunhofer overestimates the number of particles for all these low absorbing samples. For values of the relative real part of the refractive index $n = n_{\mathrm{sample}}/n_{\mathrm{medium}} = 1.1$–1.3 ($n_{\mathrm{medium}} = 1.333$ for water) and for low k (see Table 2), Mie-derived PSDs are valid for $r \geq 0.5$ μm [83]. Thus, the r_{eff} and v_{eff} values of the Mie PSD are consequently smaller than the Fraunhofer ones (Table 2). Figure 1b shows the corresponding $S(\log r)$ PSDs [65], which indicate similar projected surface area of the four samples between 1 and 10 μm.

The r_{eff} and v_{eff} values of the volcanic ash and the new desert dust samples listed in Table 2 are found to be comparable. The deficit of particles larger than 10 μm in the Sahara-OSN sample is reflected in the lower values of these parameters, similar to the Pinatubo sample. At the other extreme we find the Spurr Stop 33 sample, showing significantly higher r_{eff} and v_{eff} values due to a strong particle mode at 100 μm [75]. Regarding power law indices in the range from 1 μm to 70 μm (Table 2), the volcanic ash samples have an average power law index of $p = 3.65 \pm 0.22$. Lokon is the sample showing the largest deviation from the average, with a shallower distribution ($p = 3.01 \pm 0.10$), which deviates from a power law as a result of a bite out in the PSD between approximately 0.5 and 5 μm [74]. Although Spurr Stop 33 has a mode at 100 μm, the power law index in the 1 μm–70 μm range is close to the average. The new desert dust samples show some deviation from a simple power law, reflected in a larger uncertainty of p. The Sahara-OSN sample shows a somewhat higher slope than the rest because of its deficit in particles larger than 10 μm.

In summary, the mineral samples listed in Table 2 have similar PSDs from a scattering point of view, which justifies grouping them to obtain the average scattering properties of volcanic ash and desert dust. Moreover, the similarity in refractive indices and PSDs between the two groups may enable inspecting the influence

of factors other than size and composition (e.g. shape and structure) on their average scattering behaviour.

According to the literature, the pollen grains of the Cupressaceae family have sizes comprised between 20 and 35 μm in diameter [77]. When hydrated, grains can be as large as 40 μm, but we did not observe evidence of hydration by optical microscopy. The size of pollen grains of the sample used in the present study has been estimated both from optical microscopy images and from LLS measurements (using water as dispersion medium) as shown in Fig. 2. LLS sizing is prone to overestimating the size of grains because of the aforementioned increase in volume by water uptake and agglomeration of hydrated pollen grains. Images of cypress pollen grains obtained are shown in Fig. 2a and 2b. These grains can be characterized by a single average radius. The histogram of grain radii in Fig. 2c has been obtained from 137 cypress pollen grains and can be regarded as an estimate of the number PSD of the cypress pollen sample. The PSD obtained from LLS measurements with the Mastersizer 2000 apparatus (Fig. 2c) is broader, specially towards the large radius wing of the distribution, which is expected. Compared to the mineral samples, the cypress pollen sample is close to monodisperse, with an average radius of 11.2 μm and a standard deviation of 0.8 μm. The effective radius of the number PSD in Fig. 2b is $r_{\mathrm{eff}} = 11.4$ μm and the effective variance $v_{\mathrm{eff}} = 0.005$.

Fig. 2d indicates that the pollen sample projected surface area density is concentrated in a narrow size range at the high end of the $S(\log r)$ distribution of the mineral samples. Therefore, significant differences are to be expected between the scattering matrices of pollen grains and mineral aerosol samples simply because of size.

2.4.3. Morphology

Field-Effect Scanning electron microscopy (FESEM) images of a selection of the samples considered in this study are shown in Figs. 3, 4 and 5. The samples were collected from the aerosol jet just below the nozzle of the aerosol generator of the CODULAB setup using a small pod with a sticky surface and then metalized at the FESEM facility prior to observation. Fig. 3 shows FESEM images of a selection of the volcanic ash particles listed in Table 2. They show vesicles with sizes of 5–10 μm in diameter, consistent with size distributions reported in the literature [84], smooth surfaces and sharp edges. Micron and submicron particles often have large aspect ratios (needles, splinters). By contrast, desert dust particles
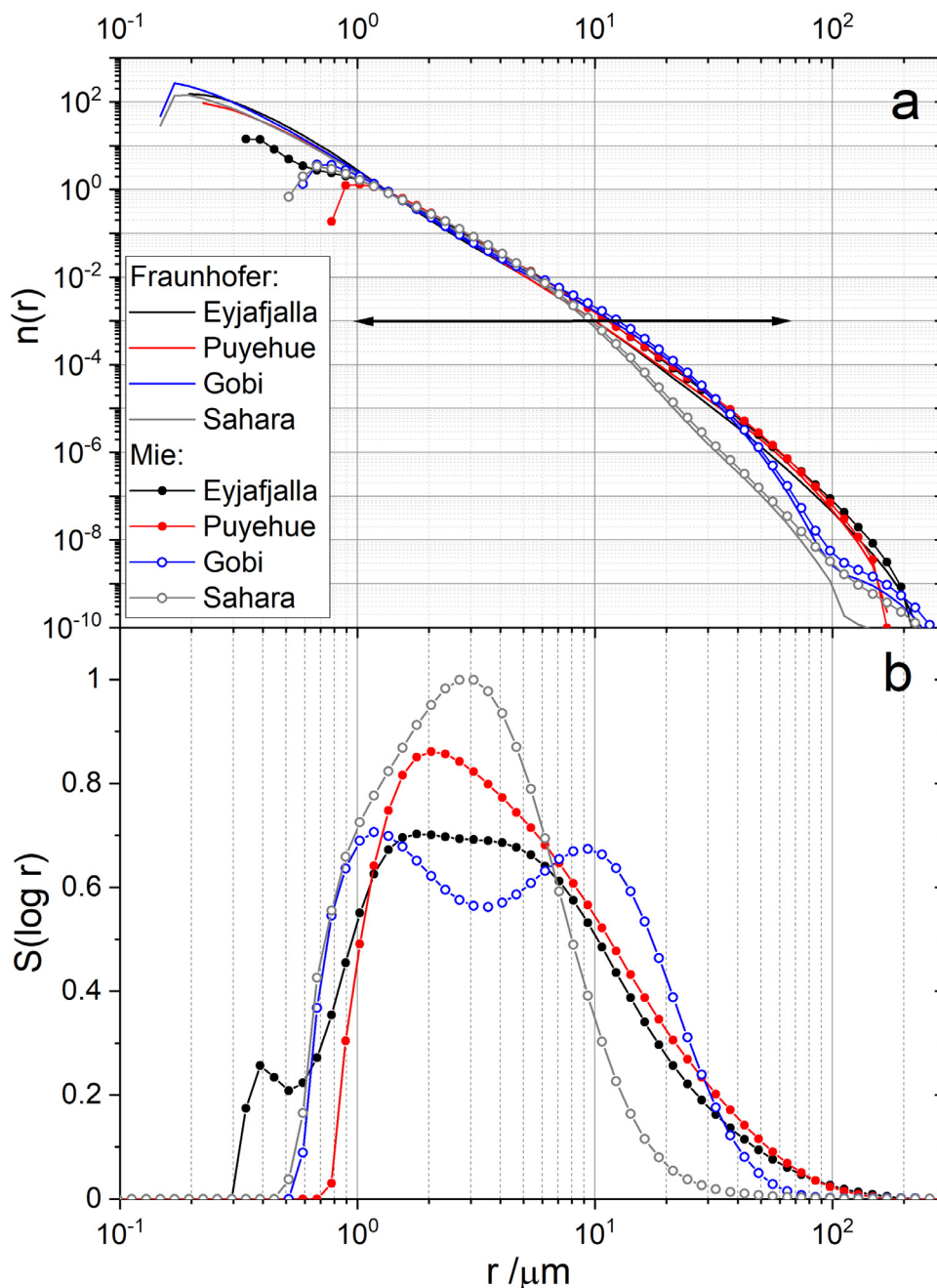
Fig. 1. Particle size distribution of the Eyjafjallajökull, Puyehue, Gobi-Beijing and Sahara-OSN samples. Panel a: Comparison of the number size distribution ($n_s(r)$) of two volcanic ash and two desert dust samples obtained using a LLS particle sizer with the Fraunhofer approximation (lines) and Mie theory (symbols). The distributions are normalized to the integral under the curve between 1 and 100 μm. The double headed arrow indicates the range of the power law fits (1 μm–70 μm). Panel b: Mie $S(\log r)$ PSDs corresponding the $n_s(r)$ PSDs in panel a. The distributions are normalized to the integral under the curve in the full log r scale range.

(Fig. 4) have no vesicles, but granulated surfaces with embedded submicron crystals. These particles have generally round edges, but some platelets and flakes can also be found. Finally, cypress pollen grains (Fig. 5) are spheroidal particles with an indentation along the major axis, showing some smooth relief on their surfaces and with submicron orbicules attached to their surface.

All the taxa within the Cupressaceae family present morphologically uniform pollen with few variations in size, shape and structure [85] (Fig. 2 is a good example of such uniformity). Pollen grains are described as spheroidal and radio-symmetric (Fig. 5a and 5b). The external layer (the exine) is slightly granular, and its surface is covered by irregularly distributed orbicules and presents concavities with diameters of the order of 5–10 μm. Fragments

with sizes larger than 1 μm were not observed neither by optical microscopy nor by FESEM, but some detached orbicules were detected in the FESEM images.

3. Results

3.1. Scattering matrix of volcanic ash

The non-zero scattering matrix elements in the red spectral range (632.8 nm and 647 nm) of all the volcanic ash samples currently in the Granada-Amsterdam database are tightly clustered in the experimentally accessible angular range (Figure S1). This results from the similar refractive index and PSDs of these samples
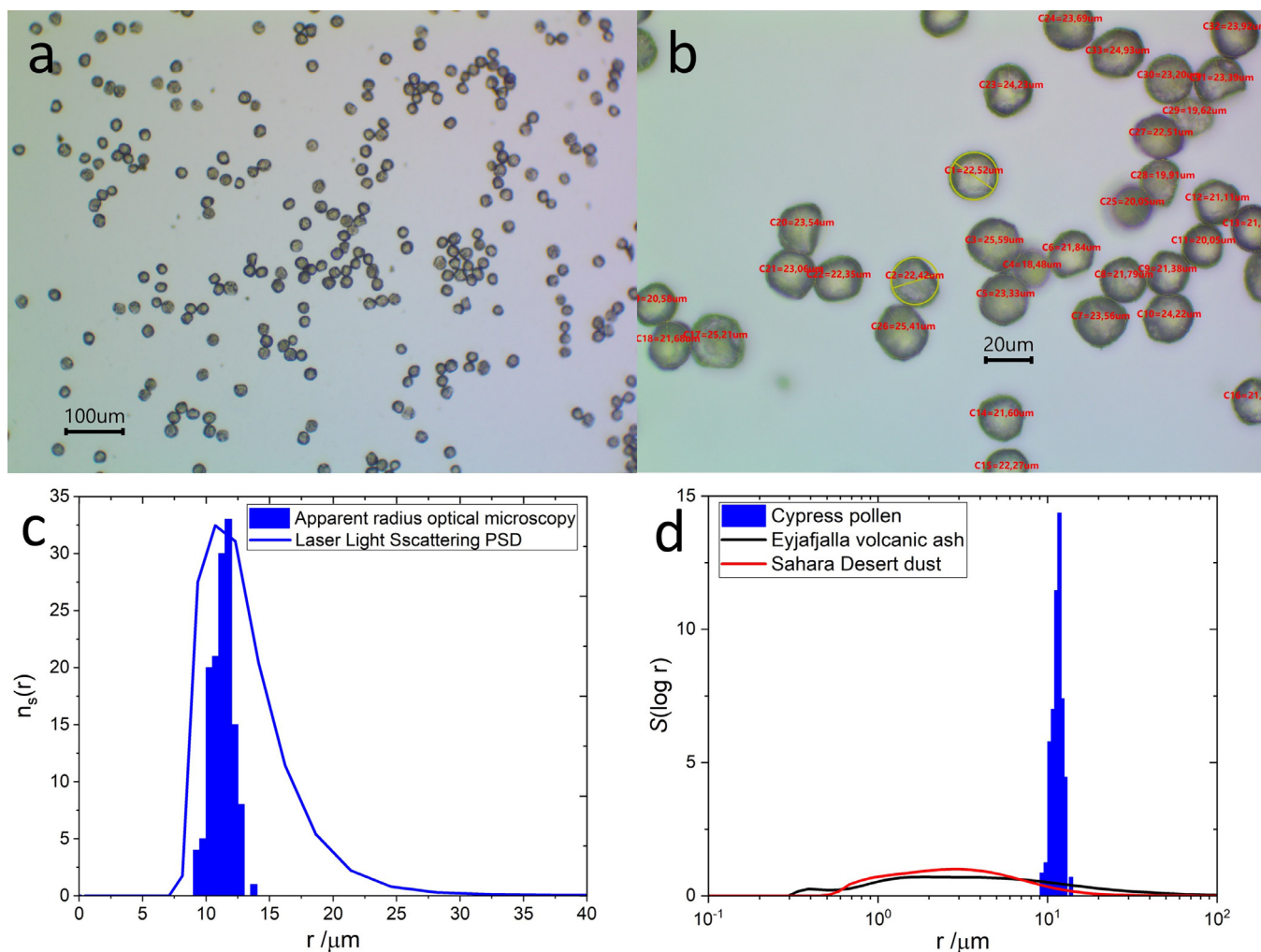
Fig. 2. Estimation of the size distribution of the cypress pollen sample. Panels a and b: Optical microscopy images (x10 and x40 magnification, respectively) of cypress pollen grains collected on a glass surface from below the aerosol generator skimmer. The contours of the cross sections of the grains (yellow lines in panel b) are approximated by circumferences (diameters of grains in red). Panel c: Estimated PSD (radius) obtained from 137 cypress pollen grains (histogram) and PSD obtained using the LLS particle sizing (blue line). Note the line linear scale in the x axis. Panel d: Comparison between the log-scale projected surface area normalized PSDs of a volcanic ash sample (Eyjafjallajökull), a desert dust sample (Sahara-OSN) and the cypress pollen sample.

and their irregular particle shapes with lack of symmetries and considerable particle-to-particle variability [75,76]. An average matrix at 632.8 nm has been previously reported, where nine samples were considered: Pinatubo, Lokon, Redoubt A, Redoubt B, Spurr Gunsight, Spurr Stop 33, Spurr Anchorage, Spurr Ashton and Mt. St. Helens [76]. The scattering matrix phase curves showing the largest deviations with respect to the mean curves are those of the Lokon sample, owing to its distinct PSD [74]. The scattering matrices for Puyehue and Eyjafjallajökull at 647 nm [76], as well as the three matrix elements of the older Chichon sample available at 632.8 nm [74], agree well with both the overall features and the magnitude of the scattering matrix elements of the other volcanic ash samples at 632.8 nm. Moreover, the non-zero scattering matrix elements in the blue spectral range (441.6 nm and 488 nm) of the Lokon, Pinatubo and Eyjafjallajökull samples are also very similar (Figure S2). The scattering matrix of the Eyjafjallajökull sample at 488 nm is reported in this paper for the first time.

We have extrapolated each of the scattering matrices in the two spectral ranges in the forward- and backscattering directions using the methodology explained in Section 2.2 and calculated the average matrix including all the available matrix elements for both wavelengths. The average synthetic matrices of volcanic ash for

red and the blue wavelengths are shown in Figs. 6 and 7, respectively. The differences in the PSD of the volcanic ash samples for $r > 70$ μm (some show a secondary mode around 100 μm) are responsible for the spread of the extrapolated forward peak for $\theta < 2$ ° (see grey shadowed regions), since this angular range of the phase function is mainly sensitive to particle size.

The average scattering matrix of volcanic ash shows typical features of polydisperse generic mineral samples [73]:

- The phase function is linear in log-log scale between 3° and 90°, approximately flat between 90° and 170° (see Figure S3 in semi-log scale), and shows a small backscatter enhancement.
- The $-F_{12}/F_{11}$ curve is bell-shaped, with a ~15% maximum at ~90° and a ~ -2% deep negative polarization branch (NPB) at backscattering angles.
- The F_{22}/F_{11} curve decreases smoothly from ~ 1 at 0° towards a minimum of ~0.3 at θ ~ 135° and then grows to ~0.4 at $\theta = 180°$.
- The F_{33}/F_{11} curve is sigmoid-shaped, decreasing smoothly from F_{33}/F_{11} ~ 1 and taking negative values for $\theta > 110°$
- The F_{34}/F_{11} element is qualitatively similar to the $-F_{12}/F_{11}$ element
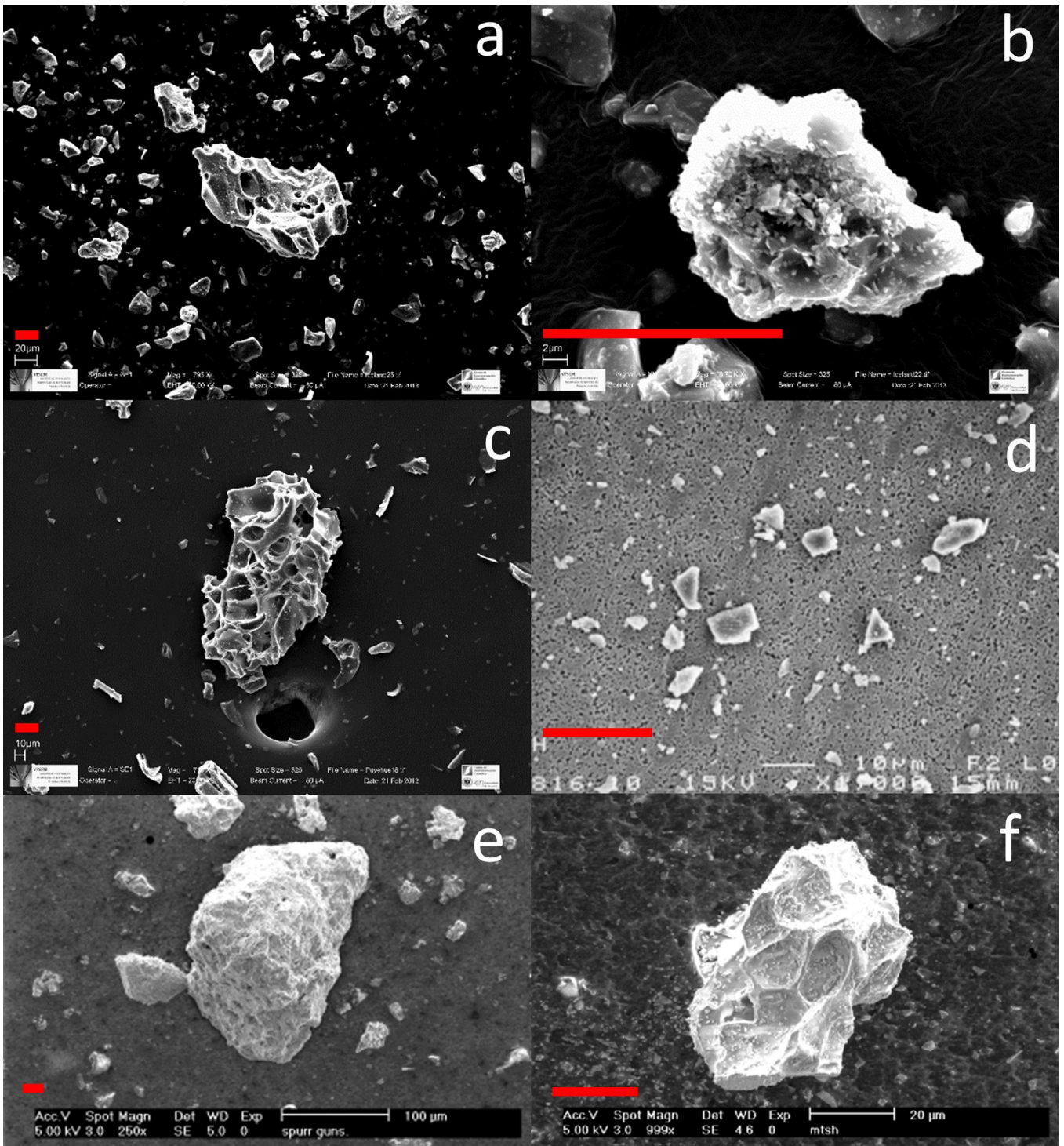
Fig. 3. Field-Effect Scanning Electron microscopy (FESEM) images of volcanic ash samples. Panel a: Eyjafjallajökull. Panel b: Eyjafjallajökull at higher resolution. Panel c: Puyehue. Panel d: Pinatubo. Panel e: Spurr Gunsight. Panel f: Mt. Saint Helens. The red bars indicate a length of 20 µm.

- The F_{44}/F_{11} element decreases smoothly from $F_{44}/F_{11} \sim 1$ at 0° towards a negative minimum of ~ -0.15 at $\theta \sim 170$ ° and then grows again. It tends to a positive value at $\theta = 180°$ given by $F_{44}(180°)/F_{11}(180°) = 1 - 2F_{22}(180°)/F_{11}(180°)$ [64], which implies a sharp backscattering enhancement in this element.

The differences between the red and the blue scattering matrices are quantitatively small and encompassed in the domain of the red matrix measurements.

3.2. Scattering matrix of desert dust

Despite the totally different origin and collection site of the desert samples, the matrix elements of the Gobi-Beijing and Sahara-OSN samples reported in this work for the first time (Figure S4) are very similar at both wavelengths, which is consistent with their similar PSDs. The scattering matrix is block diagonal as shown by Eq. (1), i.e. the measured matrix elements F_{13}, F_{14}, F_{24}, F_{31}, and F_{41} are zero as for the volcanic samples, which confirms
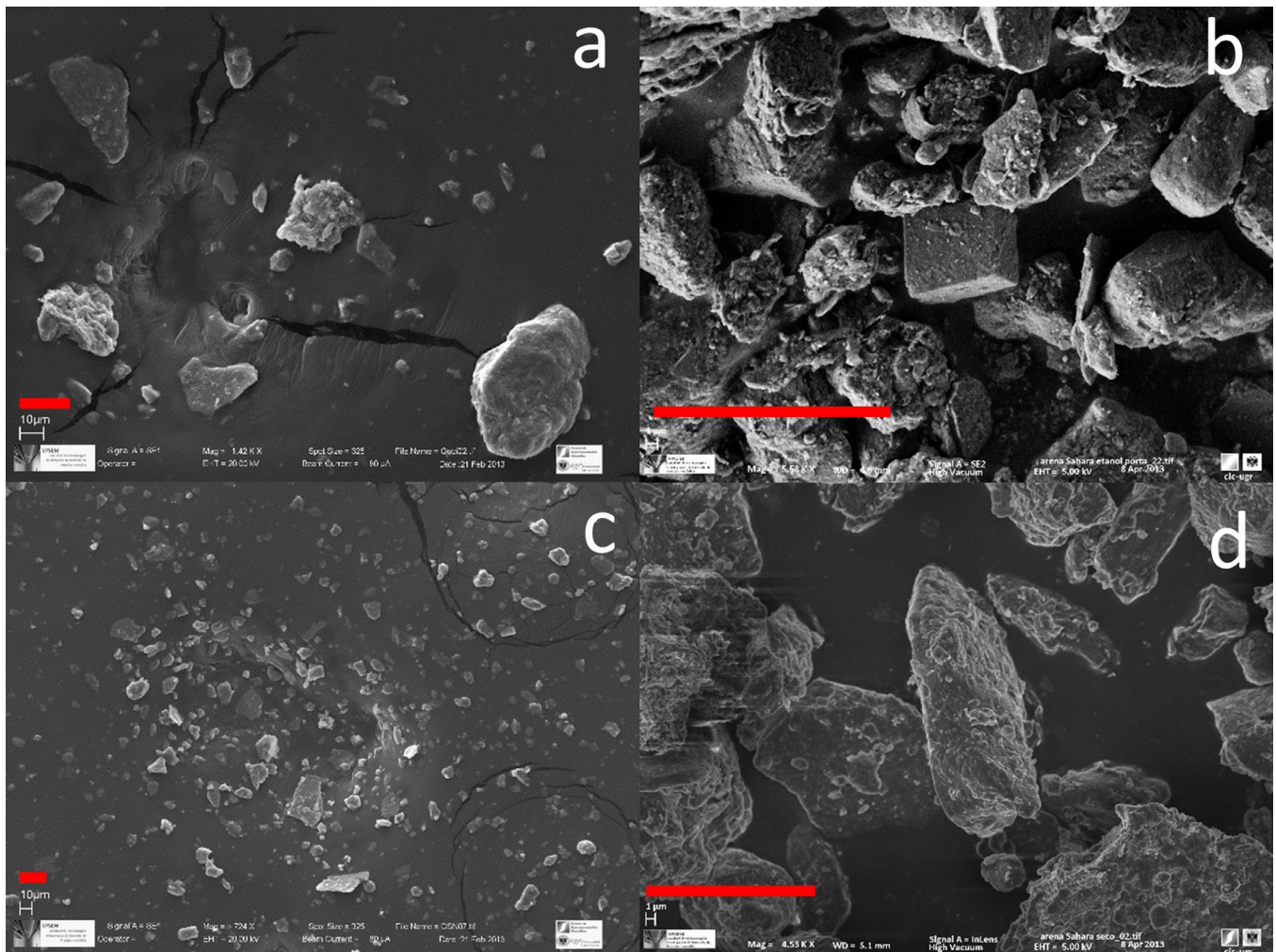
Fig. 4. Field-Effect Scanning Electron microscopy (FESEM) images of desert dust samples. Panel a: Gobi-Beijing. Panel b: Gobi-Beijing at a higher resolution. Panel c: Sahara-OSN. Panel d: Sahara-OSN at a higher resolution. The red bars indicate a length of 20 μm.

the assumption of mirror symmetry of the ensemble and randomly oriented particles. Qualitatively, the phase curves are similar to those of volcanic ash and other mineral aerosols. The average extrapolated scattering matrices of the two desert dust samples have been calculated in the same manner than for volcanic ash. Figs. 6 and 7 show the average non-zero matrix elements for desert dust in the red and the blue, respectively.

3.3. Pollen

The non-zero elements of the scattering matrix of the cypress pollen sample in the green (514 nm) are plotted in both Figs. 6 and 7 for comparison with the red and blue scattering matrices of the mineral samples. Again, the measured off-diagonal block elements are zero as for other samples and are not shown. The different refractive index, PSD and geometry of the pollen sample compared to the mineral samples result in markedly different scattering matrix element curves. The most striking features of the cypress pollen scattering matrix are the qualitative similarities with the phase function and DLP curves of spheroids [86] (see Figure S5). Both the DLP and the F_{34}/F_{11} curves show two negative branches.

Note that because the PDS is extremely narrow and we assume spherical particles, the extrapolated near-forward range of pollen shows resonance features. Because of their near-spheroidal shape, with a relatively low aspect ratio, secondary lobes may in-

deed exist [64,86–88], but probably not as sharp as the one appearing in the extrapolated curves shown in Fig. 6 and 7 (see also Figure S5).

3.4. Comparison of the average scattering matrices of volcanic ash samples, desert dust samples and the cypress pollen sample

The phase functions of volcanic ash and desert dust in forward-to-side scattering ($3° < \theta < 90°$) are remarkably similar, with power law dependence on scattering angle [89] and a narrow spread. By contrast, the cypress pollen phase function is not linear in log-log scale (see Fig. 6). In side-to-backscattering ($90° < \theta < 180°$), the phase functions of volcanic ash and desert dust are also similar, reaching a broad minimum around 140°–150°. The backscattering enhancement with respect to the minimum is slightly larger for desert dust. The cypress pollen phase function reaches its minimum at 100° and the increase towards backscattering is less steep, although the backscattering enhancement with respect to this minimum is higher than for the mineral samples.

The DLP of volcanic ash and desert dust are very similar in the full scattering angle range. The range of variability of volcanic ash samples encompasses the average desert dust curve. In near-backscattering, the desert dust curve appears to have a shallower negative polarization branch (NPB) and a higher inversion angle. The Cypress Pollen DLP phase curve is remarkably different from those of mineral samples, showing a negative branch at
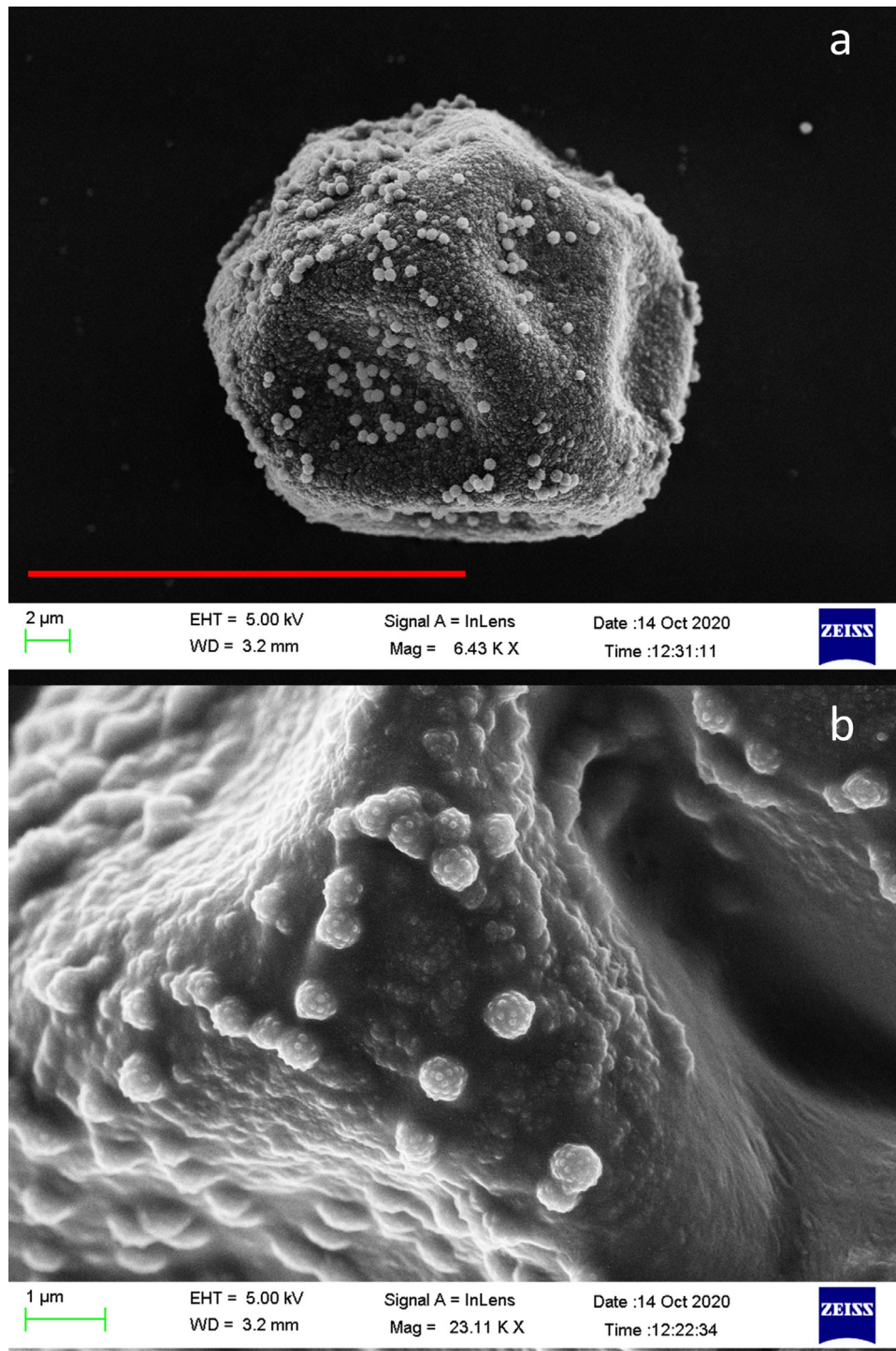
Fig. 5. Field-Effect Scanning Electron microscopy (FESEM) images of the cypress pollen sample. Panel a: Full cypress pollen grain. Panel b: Detail of the cypress pollen grain in panel a showing orbicules attached to the exine's surface. The red bar indicates a length of 20 μm.

forward-to-side scattering with minimum at 60°. In side-to-backscattering the DLP phase curve of Cypress pollen has a similar slope that that of the mineral samples, but the inversion angle and the angle of the backscattering NPB minimum are significantly lower than for mineral samples.

Regarding the F_{22}/F_{11} element, the volcanic ash and cypress pollen samples overlap over most of the angular range, although the minimum of the pollen curve is higher. The desert dust curve appears to be consistently lower. The three curves converge in backscattering at a similar value of approximately 0.43, which im-

plies also very close values of the depolarization ratios at 180° of the three samples (listed in Table 3 and plotted in Fig. 8), despite of their different nature. Because of the smooth variation of F_{22}/F_{11} and the near zero values of $-F_{12}/F_{11}$ in near-backscattering, a measurement of δ_L at $(173° \leq \theta < 180°)$ is still a good approximation of the value at exact backscattering, in case the latter is not accessible experimentally (see Table 3 and Fig. 9, panel b).

The volcanic ash and cypress pollen samples overlap in most of the angular range of the F_{33}/F_{11} phase curve. The desert dust curve appears to be consistently lower in forward to side
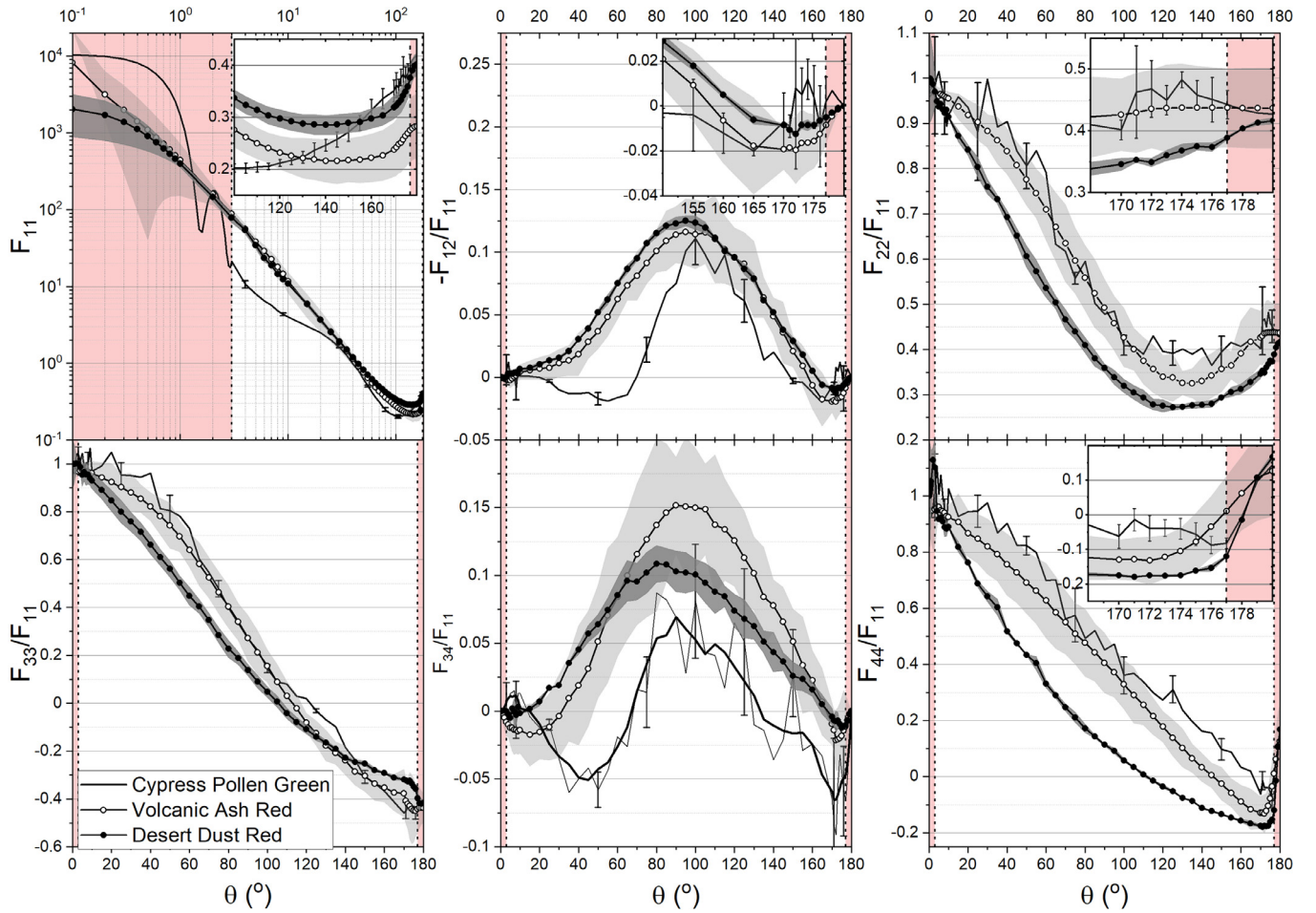
Fig. 6. Non-zero average scattering matrix elements in the red (632.8 nm–647 nm) of clouds of randomly oriented airborne natural aerosol samples collected outdoors: volcanic ash (empty circles) and desert dust (full circles). The grey shaded areas enveloping each averaged curve indicate the range of the data entering the averages. The scattering matrix elements of cypress pollen measured in the green (514 nm) are also shown (solid lines), with error bars indicating experimental uncertainty (shown every five angles for clarity). Note that for the F_{34}/F_{11} matrix element of cypress pollen a five-points moving average smoothing is applied to guide the eye (thick solid line). The shaded red regions indicate the scattering angle ranges where measurements could not be carried out and the curves have been extrapolated to 0° and 180° (see section 2.2). The zoomed inset plots of each panel show the backscattering region of each matrix element.

Table 3
Backscattering depolarization ratios.

	$r_{eff}/\mu m$	v_{eff}	λ/nm	$\delta_L(173°)$	$\delta_L(180°)$	$\delta_C(173°)$	$\delta_C(180°)$	$\delta_C(180°) - \delta_C(173°)$
Volcanic ash	6.0	7.6	442–488	0.35 ± 0.01	0.37 ± 0.05	0.70 ± 0.07	1.2 ± 0.3	0.50 ± 0.13
			633–647	0.38 ± 0.07	0.39 ± 0.07	0.78 ± 0.10	1.3 ± 0.3	0.52 ± 0.15
Desert dust	3.8	2.8	488	0.43 ± 0.01	0.41 ± 0.02	0.67 ± 0.01	1.41 ± 0.06	0.70 ± 0.02
			647	0.46 ± 0.02	0.41 ± 0.02	0.70 ± 0.03	1.40 ± 0.06	0.70 ± 0.03
Cypress pollen	11.4	0.005	514	0.38 ± 0.02	0.40 ± 0.03	0.93 ± 0.04	1.34 ± 0.05	0.41 ± 0.02

scattering ($0° < \theta < 100°$). For this element the differences between the three types of aerosol are small.

In forward-to-side scattering (0° to ~90°), the range of variability of the F_{34}/F_{11} curves of volcanic ash samples encompasses most of the average desert dust curve, but the shapes appear to be different and, most importantly, the desert dust curve does not show negative values. Also, the maximum of the desert dust curve is lower and peaks at a lower angle. The cypress pollen F_{34}/F_{11} phase curve is noisy, but it is still possible to see its striking differences from the curves of the two mineral samples: a deep negative branch at forward-to-side scattering with a minimum at 50°, and a lower maximum. Between 90° and 180°, the F_{34}/F_{11} phase curves of volcanic ash and desert dust have different decreasing slopes and converge at a similar inversion angle. The desert dust

curve has a shallower near-backscattering negative branch. The cypress pollen F_{34}/F_{11} phase curve has a similar slope to the desert dust one, but the inversion angle and the angle of the side-to-back negative branch minimum are lower than for mineral samples, and the minimum is deeper.

Finally, the F_{44}/F_{11} phase curves of volcanic ash and cypress pollen overlap between 0° and 100°, and the desert dust curve is consistently lower, which is similar to the relative behavior of the F_{22}/F_{11} curves. Between 100° and 180°, the pollen curve appears to be higher than the volcanic ash curve (outside the variability range), and the desert dust curve is still consistently lower. This is similar to the relative behavior of the F_{22}/F_{11} curves in the 120°-170° range. The three F_{44}/F_{11} curves converge at a similar value of approximately 0.15 at 180°, because of the convergence of the
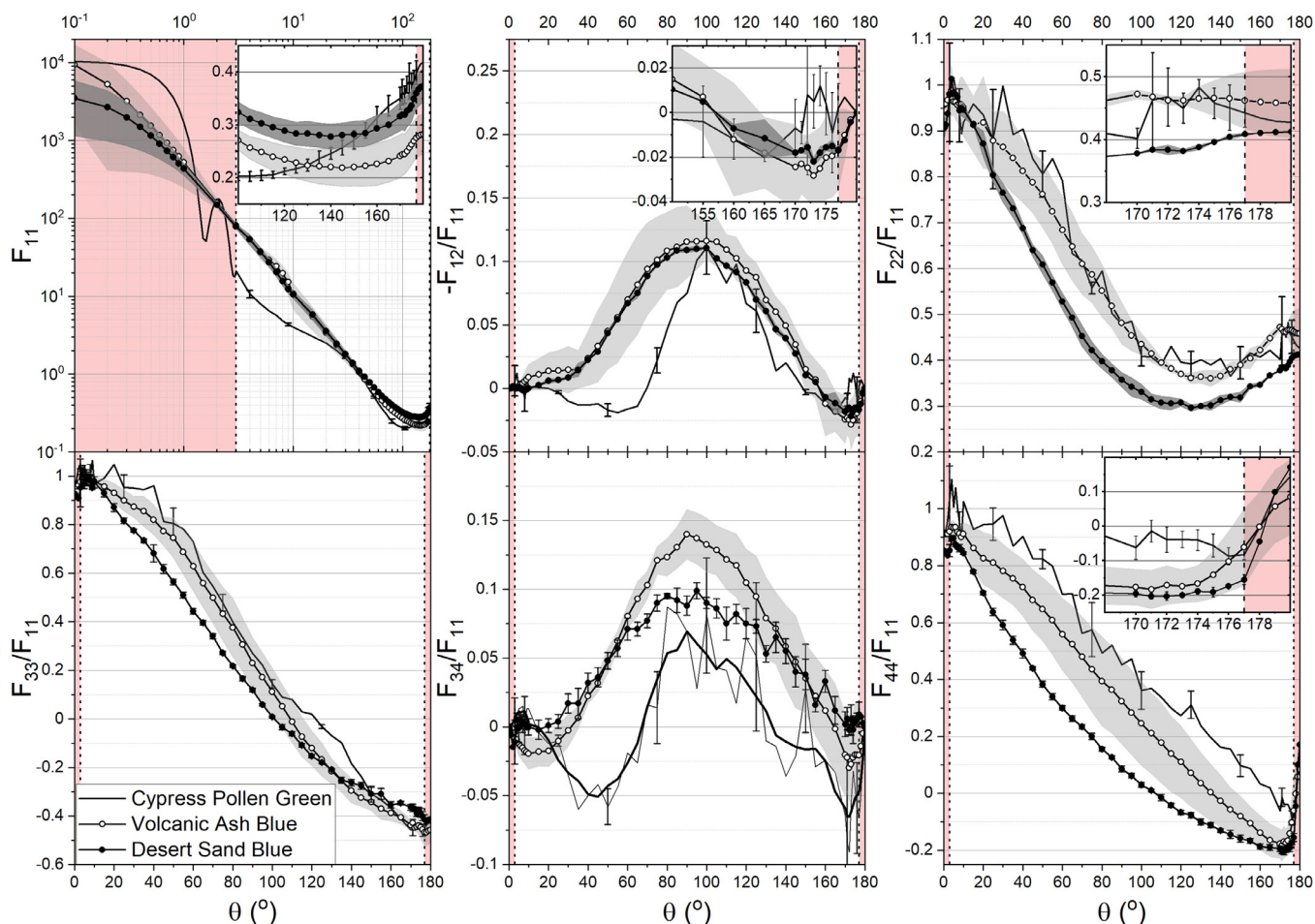
Fig. 7. As Figure 6 but for the average scattering matrix elements of volcanic ash and desert dust in the blue (441.6 nm–488 nm). The scattering matrix elements of cypress pollen in the green are also shown as in Fig. 6. For desert dust, the elements F_{33}/F_{11}, F_{34}/F_{11} and F_{44}/F_{11} were measured only for one sample (Gobi-Beijing). Hence, the error bars for these matrix elements of desert dust show the experimental uncertainty of the only curve available.

F_{22}/F_{11} and the mirror symmetry condition $F_{44}(180°)/F_{11}(180°) = 1 - 2F_{22}(180°)/F_{11}(180°)$. This also implies similar values of circular depolarization at 180° for the three samples. It is worth noting that the sharp increase of the F_{44}/F_{11} curve from a negative minimum around 173° to a positive value at 180° deduced from mirror symmetry is genuine, since the trend is visible in the measured data up to 177°. Differences between δ_C at 173° and 180° are listed in Table 3 and plotted in Fig. 9.

Although less samples are available in the blue than in the red for the volcanic ash (three) and the desert dust (two for the first three elements, but just one for the rest), the relative behavior of the scattering matrix element phase curves at both wavelengths is very similar. The main difference with the curves of mineral samples in the red is that there is a stronger contrast between volcanic ash and pollen for the F_{22}/F_{11}, F_{33}/F_{11} and F_{44}/F_{11} elements. The pollen curves of these elements are higher and fall now mostly outside of the variability range of the volcanic ash curves. However, the F_{22}/F_{11} and F_{44}/F_{11} elements (and the depolarization ratios, see Table 3) converge similarly at 180°.

4. Discussion

Some laboratory studies reporting polarization properties of mineral and biological aerosols focus on linear depolarization at the backward or near backward scattering direction [30,61,90]. This is because this quantity can be measured with lidars and is used to distinguish between spherical and non-spherical aerosol and cloud particles and hydrometeors [91,92]. For instance, Järvinen et al. [61] carried out environmental chamber depolarization lidar measurements at near-backscattering of a vast variety of aerosol samples with narrow PSDs and small median volume radius ($r < 1.5$ μm). These experiments indicate that for irregularly-shaped particles, δ_L increases with increasing aerosol size up to a radius of 0.5 μm (size parameter $x = 2\pi r\lambda^{-1} \sim 6$), where δ_L reaches a plateau of about ~ 0.3, independently of the nature of the aerosol. Light scattering models using spheroids as model particles with an average complex refractive index are capable of reproducing the main trend of this δ_L data ensemble formed by a range of different particulate materials [93]. Hence, δ_L at backscattering can be used to discriminate between fine ($r < 0.5$ μm) and coarse ($r > 0.5$ μm) atmospheric aerosol, but it does not provide a criterion to distinguish between different types of aerosol. Field measurements of the backscattering linear depolarization ratio of airborne dust (see e.g. Table 1 of Kahnert et al. [93]) are in general somewhat lower ($\delta_L = 0.30$–0.35) than the values in Table 3 ($\delta_L \sim 0.4$), although it must be kept in mind that the presence of smaller or more spherical particles in airborne clouds may result in smaller values of δ_L.

The backscattering depolarization ratios of the volcanic ash, desert dust and pollen samples determined in the present study are the same within sample variability and experimental error. The average for the three types of aerosols in the visible spectra range is $\delta_L(180°) = 0.40 \pm 0.05$, which agrees with other measurements of similar samples (Fig. 8). Therefore, this parameter cannot be

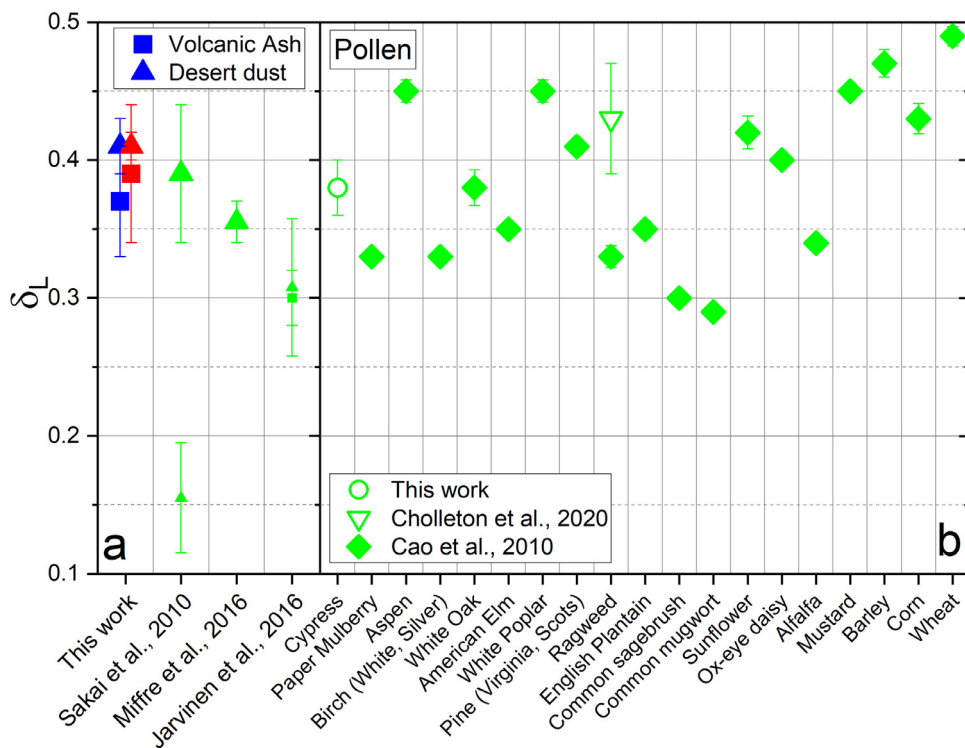**Fig. 8.** Linear depolarization ratios δ_L obtained in this work compared to depolarization ratios from laboratory measurements reported in the literature for volcanic ash, desert dust and pollen. Panel a: δ_L of volcanic ash (squares) and desert dust (triangles). Panel b: δ_L for different types of pollen. Symbol colors (blue, green and red) denote the wavelength range at which measurements where performed. Symbols sizes (small, large) denote the size of the particles (submicron, micron).

used to distinguish between these types of aerosol, not even regarding size. The PSDs of these samples, which are representative of major types of airborne aerosol, contain a significant fraction of micron-sized particles, and the linear polarization ratios are within the range expected for such particle sizes (Fig. 9, panel a). The PSD of the cypress pollen sample is very narrow, but this does not have any consequence for the value of $\delta_L(180°)$.

Another parameter that can be measured by lidar is the circular depolarization ratio δ_C. In the backscattering direction, $\delta_C(180°)$ is linked to $\delta_L(180°)$ if the particles are randomly oriented and present mirror symmetry [64], which has been confirmed experimentally [72]. Thus, such measurement can be performed if there is a suspicion that particles may not fulfill these conditions [61], but airborne mineral particles and PBAP usually meet them, rendering the circular depolarization ratio measurements somewhat redundant. Near-backscattering δ_C has been shown theoretically to be dependent on particle size [94]. Bi-static lidar measurements of δ_C at different scattering angles [95] could provide a more sensitive method for classification of particles by size than measuring δ_L, since as shown in Fig. 9b, the difference between near-backscattering (173°) and exact backscattering δ_C increases with r_{eff}. The variation of this curve samples better the region where the traditional cut-off between fine and coarse particles is found (2.5 μm), compared to δ_L. Nevertheless, this criterion is not helpful for the three samples under study here, since all of them lie at the high side of the sigmoid function that empirically fits the δ_L versus r_{eff} curve.

For the purpose of distinguishing between different major types of atmospheric aerosol, the capability of measuring several scattering matrix elements at different scattering angles, and not just the backscattering direction, appears to be mandatory. Hierarchical cluster analysis of a selection of measurements in the red spectral range (except for the pollen measurements in the green) of $F_{11}(90°, 130°, 170°)$, $-F_{12}/F_{11}$ (60°, 90°, 160°), F_{22}/F_{11}(60°, 90°, 130°),

and F_{44}/F_{11} (60°, 90°, 170°) of the samples in Fig. 9b plus a few more samples from the Granada-Amsterdam database [60] and the cypress pollen sample reported here has been carried out in order to illustrate this point. The scattering angles have been selected based on the occurrence of the most distinct features of each scattering matrix element described above, but there is room for optimization of the scattering angles at which measurements are performed [98]. The matrix elements selected are those that are related to measurements performed by field instruments. The phase function is employed with the usual $F_{11}/F_{11}(30°)$ normalization of the Granada-Amsterdam database.

Hierarchical clustering analysis has been performed using both the Matlab and Origin built-in clustering tools [99,100], which give the same results. The analysis performed here uses the group average method and the Euclidian distance, which is calculated as the average distance between all pairs of objects in the different clusters [101]. As a result of this exercise, the data can be classified according to the selected variables in eight major clusters for a minimum inter-cluster distance of 0.3 (see the *dendrogram* in Fig. 10), with a cophenetic correlation coefficient $c = 0.803$ (see chapter 14 of reference [101] for description of this quality metric and further details about hierarchical clustering analysis). Five of these clusters are composed of just one member: rutile, hematite, cypress pollen, Feldspar and Fly ash. One of the other three groups contains volcanic ash, and the other desert dust. The inclusion of the three F_{11} variables does not result in major changes of the distances between volcanic ash, desert dust and pollen, but it does change the distances between other samples and, as a consequence, the distribution of clusters. This can be appreciated in Table 4, which lists the mutual distances between volcanic ash, desert dust and cypress pollen calculated including and excluding the three F_{11} variables in the cluster analysis, as well as the number of clusters for a cut-off inter-cluster distance of 0.3. When the only variables used are F_{11} (90°, 130° and 170°) and $-F_{12}/F_{11}$ (60°, 90°, 160°), the
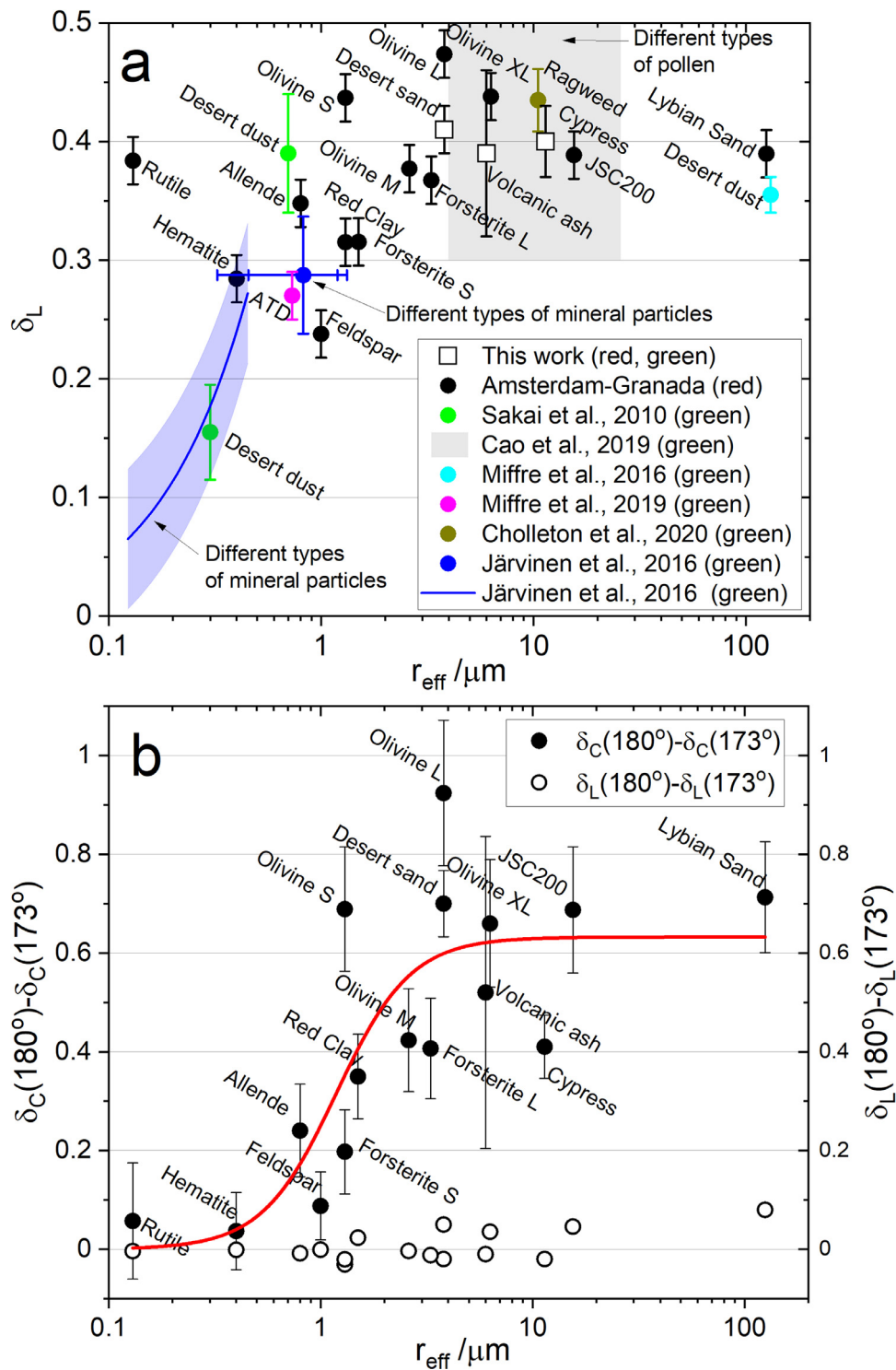
Fig. 9. Panel a: backscattering δ_L of irregular mineral particles calculated from literature scattering data, including Granada-Amsterdam scattering matrices extrapolated with the method outlined in Section 2 (black dots) and data from other references [30,61,72,90,96,97]. The data from Järvinen et al. [61] has been divided in two regions. For $r_{eff} < 0.5$ μm, a linear fit of the data is presented, with the variability region indicated by a shaded area. For 0.5 μm $< r_{eff} < 1.55$ μm, the average and standard deviation are presented. For the narrow distributions considered by Järvinen et al. the volume modal radius is very close to r_{eff}. All the δ_L at exact backscattering except data from Järvinen et al. [61] (178°), Cholleton et al. [96] (178°), and Sakai et al. [90] (178.8°–179.6°). Panel b: Differences between backscattering (180°) and near-backscattering (173°) circular and linear depolarization ratios (left and right axis, respectively) in the red spectral range for samples in the Granada-Amsterdam database and this work (pollen only exception in the green). The red line is an empirical sigmoidal fit through the black dots.
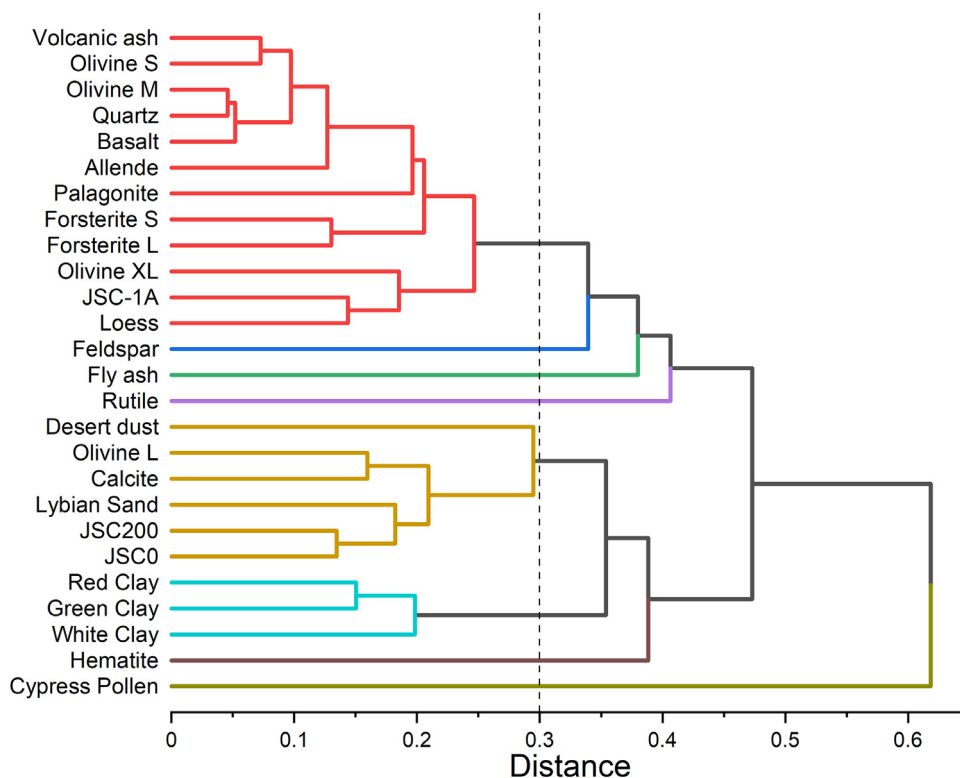
Fig. 10. Dendrogram obtained from hierarchical cluster analysis of a set of twelve variables F_{11} (90°, 130°, 170°), F_{12}/F_{11} (60°, 90°, 160°), F_{22}/F_{11}(60°, 90°, 130°), and F_{44}/F_{11} (60°, 90°, 170°) for 26 aerosol samples (i.e. the observations), including the three types discussed in the present study and a selection of samples from the Granada-Amsterdam database. The clustering uses the group average method and the Euclidian distance. F_{11} is normalized to F_{11}(30°). Variables are not standardized before clustering. The colors identify the eight different clusters defined by the 0.3 distance cut-off.

Table 4
Hierarchical cluster analysis: distances between the samples listed in Fig. 10 and number of clusters obtained when different sets of variables are considered.

	Distances [b]						Number of clusters[c]	
	Volcanic ash-Desert dust		Volcanic ash-Cypress pollen		Desert dust-Cypress pollen			
Elements analyzed [a]	with F_{11}	w/o	with F_{11}	w/o	with F_{11}	w/o	with F_{11}	w/o
$-F_{12}/F_{11}$, F_{22}/F_{11}, F_{44}/F_{11} [d]	0.50	0.49	0.51	0.50	0.68	0.68	8	7
$-F_{12}/F_{11}$, F_{22} F_{11}	0.23	0.23	0.50	0.49	0.46	0.45	4	2
$-F_{12}$ F_{11}, F_{44}/F_{11}	0.44	0.44	0.17	0.14	0.52	0.52	5	3
$-F_{22}/F_{11}$, F_{44}/F_{11}	0.50	0.49	0.50	0.49	0.67	0.67	7	5
F_{22}/F_{11}	0.23	0.22	0.49	0.48	0.45	0.44	3	2
F_{44}/F_{11}	0.44	0.44	0.15	0.11	0.51	0.50	3	2
$-F_{12}/F_{11}$	0.06	0.02	0.13	0.09	0.13	0.10	1 [e]	1
none	0.06		0.10		0.08		1	

[a] For each element, 3 scattering angles are considered (see text). [b] Bold typescript indicates that the two samples belong to different clusters according to the 0.3 cut-off distance criterion. [c] Number of clusters for a cut-off distance of 0.3 (see Fig. 10). [d] This case corresponds to the dendrogram in Fig. 10. The maximum distance between two samples is 0.83 (feldspar-desert dust), while the maximum distance between two clusters is 0.72 (rutile cluster – clay cluster). [e] Two distinct clusters appear if the cut-off is relaxed to 0.22, one containing the 'singular' samples (pollen, hematite, rutile, feldspar, fly ash), and another one containing the rest of the samples.

distance between volcanic ash and desert dust is significantly shorter, as shown in Table 4, and they can be clustered together. Similarly, when the only variables used are F_{11} (90°, 130° and 170°) and F_{44}/F_{11} (60°, 90°, 160°), volcanic ash and cypress pollen are very close. Thus, some combinations of angular measurements of two of the three elements $-F_{12}/F_{11}$, F_{22}/F_{11} and a F_{44}/F_{11} (Table 4 shows the distances between the three samples for different combinations of variables analyzed) provide enough distance for differentiation of volcanic ash, desert dust and a specific type of pollen (cypress). The phase function is the default measurement in many field instruments, but as Table 4 shows it adds little information to the classification of samples (it adds key particle sizing information in the forward-to-side scattering angle range). Regarding pollen, full scattering matrix measurements of different taxa are needed to see what elements may be useful to distinguish between

pollen types, which show a range of shapes and sizes, as well as to find some common characteristics that may allow constructing an average dataset analog to the ones discussed in this paper for volcanic ash and desert dust.

The pool of variables analyzed could be expanded with measurements in the blue spectral range for a subset of samples of the Granada-Amsterdam database for which both blue and red wavelength measurements are available. Including blue wavelength measurements of F_{11}(90°, 130°, 170°), $-F_{12}/F_{11}$ (60°, 90°, 160°), F_{22}/F_{11}(60°, 90°, 130°), and F_{44}/F_{11} (60°, 90°, 170°) in the analysis (24 variables) results in essentially the same clusters shown in Fig. 10. Restricting the analysis to the F_{11} and $-F_{12}/F_{11}$ variables (six red + six blue) yields four clusters, i.e. including the blue measurements enhances the dissimilarity between the samples compared to the poorer result obtained with only six red wavelength

variables (Table 4, next to last row). More interestingly, the analysis can be applied to near-backscattering measurements at two wavelengths: F_{11} (173°, red), F_{11} (173°, blue), F_{22}/F_{11}(173°, red), F_{22}/F_{11}(173°, blue), F_{44}/F_{11}(173°, red) and F_{44}/F_{11}(173°, blue), which would be closer to the kind of measurements performed by a two-wavelength backscattering lidar. The resulting dendrogram (Figure S5) shows four well differentiated groups. Although, desert dust and volcanic ash belong to the same group, three other groups are found (clays, JSC Martian analogs and fly ash). This highlights the importance of carrying out measurements at several wavelengths, which in some cases may help to discriminate between some types of aerosols [97].

The analysis above suggests that addition of $F_{22}(\theta)/F_{11}(\theta)$ and $F_{44}(\theta)/F_{11}(\theta)$ channels (or linear and circular depolarization ratios) to active remote sensing and in situ detection devices likely would provide contrast to tell apart different types of aerosol. Passive remote sensing devices rely on incident unpolarized sunlight, which in principle precludes the determination of matrix elements other than $F_{11}(\theta)$ and $-F_{12}(\theta)/F_{11}(\theta)$. Even so, ground-based DLP observations by radiometers are rather limited [22]. Adding DLP variables increases in our analysis the distance between desert dust and pollen with respect to the phase function-only case (note the difference between the pollen and the desert dust DLP curves in Figs. 6 and 7), and in fact it is known that DLP measurements are helpful for retrieving aerosol optical and microphysical parameters [22]. In general, machine learning trained on scattering laboratory or modeling data may be a useful addition to having measurements of several elements of the scattering matrix [98,102]. As a caveat to this discussion, note that some a priori knowledge about the dominant aerosol population is needed in order to interpret aerosol light scattering field observations since, except for the separation of spherical and irregular particles, mixtures of irregular particles cannot yet be disentangled.

The physical reasons for a classification such as the one in Fig. 10 are not straightforward. On the one hand, the separation of pollen, rutile, hematite, feldspar and fly ash in one-member groups is clear, based on their specific PSDs (pollen, hematite, rutile, feldspar), refractive indices (hematite and rutile) and shape (fly ash, rutile) (see https://www.iaa.csic.es/scattering). Furthermore, the three types of clays are grouped together, which can be understood because they have almost identical PSDs and optical constants, and inspection of the high quality FESEM images of green and white clay indicates that their particles have the same structure. But on the other hand, the membership to the volcanic ash and desert dust groups is difficult to trace to physical properties of particles (it is not related to effective radius and variance nor to refractive index). Desert dust is according to the clustering analysis, the less representative observation of its group (dark yellow in Fig. 10) and may well be classified as a one member separated cluster by a very small reduction of the distance cut-off. Inspection of the FESEM images of the samples listed in Fig. 10 (see https://www.iaa.csic.es/scattering), including those in Fig. 3 and 4 suggest four types of particle surfaces: (i) layered particles (calcite and clays), (ii) compact aggregates with generally rounded surfaces (desert dust, JSC-0, JSC-200), (iii) chunks with some sharp edges (olivines, forsterites, Allende, loess, palagonite, quartz, basalt) and (iv) vesiculated particles with smooth surfaces and their compact, smooth and somewhat angular fragments (volcanic ashes, JSC-1A). The basalt sample shows some mixing between types (ii) and (iv) and the Libyan sand is a case on its own, with very large rounded, compact particles with rough surfaces composed of small grains at the submicron scale. We note that in type (iv) particles, vesiculation is present to different extents in the largest particles (Fig. 3). A size distribution of vesicles exists, centered around 5–10 μm in diameter [84], but the backbone of these particles and their fragments of 2–3 μm, where the projected surface distributions peak (Fig. 1), are essentially compact and smooth, somewhat angular particles. Interestingly, types (i) and (ii) are mostly clustered in the desert dust branch of the cluster analysis in Fig. 10, while types (iii) and (iv) are mostly linked to volcanic ash, with the apparent exception of the Olivine L sample. Thus, the differences of the scattering matrix elements of volcanic ash and desert dust, and their related samples, appear to be caused by surface structure with characteristic dimensions of 1 μm and smaller, be it layered plates or round monomers.

Merikallio et al. [76] showed that an equiprobable shape distribution of ellipsoids does a good job as a model for reproducing the scattering matrix elements F_{11}, $-F_{12}/F_{11}$, F_{33}/F_{11} and F_{44}/F_{11} of volcanic ash, at least in terms of the general shape of the phase. But on the other hand, they found F_{22}/F_{11} and F_{34}/F_{11} difficult to replicate, which in the light of the discussion above may be understood in terms of the sensitivity of these two matrix elements to surface structure. Although ellipsoids are applied successfully to retrieve several physical parameters of atmospheric aerosol such as size and refractive index from radiometric and polarimetric observations [18,19], identification of the nature of the aerosol cannot be done with such a simple shape. Lindqvist et al. [103] performed DDA calculations with vesiculated model particles and found qualitatively agreement between the simulations and laboratory measurements of F_{11} and $-F_{12}/F_{11}$ for volcanic ash, although the agreement was poor for F_{22}/F_{11}, keeping in mind that DDA calculations cannot be run for the complete size range of the real samples. Large vesicles (compared to particle size) were found to produce similar scattering results than surface structure, which is consistent with the observation of similar F_{22}/F_{11} for all types of volcanic ash and for compact particles.

Modelled scattering matrices of pollen grains are restricted to some specific shapes [104] and have not been previously compared with laboratory measurements. Prolate ellipsoids with the same size distribution and similarly low aspect ratio ($a/b = 1.2$) than the cypress pollen grains show a dip in F_{11} and correspondingly high $-F_{12}/F_{11}$ and F_{22}/F_{11} values at side-to-back scattering, according to our ray-tracing calculations using the geometric-optics approximation [86] (Figure S6). The low aspect ratio of the spheroids results in scattering features reminiscent of those of spherical particles. The enhanced F_{11}, lower $-F_{12}/F_{11}$ and F_{22}/F_{11}, and smoother angular dependence of the three elements at side-to-back scattering angles shown by the pollen particles relative to the ellipsoid model are caused by their irregular shape and surface roughness. For a larger aspect ratio ($a/b = 2$), the calculated values for ellipsoids are closer to the measurements in some sections of the curves (e.g. side scattering), but farther away in other angular ranges. Averaging over an aspect ratio distribution would smooth out the narrow features shown by the calculated curves, potentially bringing them closer to the observations [105]. However, the pollen grains have a very narrow aspect ratio distribution (see Fig. 2), which suggests that the size and aspect ratio-averaged F_{11}, $-F_{12}/F_{11}$ and F_{22}/F_{11} values for spheroids will still be far from the measured curves at side-to-back scattering. It is well known that the success of the spheroid model in reproducing the F_{11} and $-F_{12}/F_{11}$ scattering elements of irregular particles usually implies unrealistic shape distributions [105,106]. This suggests that scattering matrix measurements of quasi-monodisperse irregular particles such as the cypress pollen grains considered in this work could provide a more stringent benchmarking test for size distribution retrieval inversion algorithms based on ellipsoids than the scattering matrices of polydisperse samples.

5. Summary and conclusions

In this work, average scattering matrices of volcanic ash and desert dust have been constructed from existing and new

measurements carried out with particle samples collected in the field and representative of natural airborne aerosols. These old and new samples present remarkably similar refractive indices and size distributions, which enables calculation of average matrices for these two major types of atmospheric aerosol. Before averaging, the individual matrices have been extrapolated to the forward and backscattering directions using an updated extrapolation procedure which takes advantage of mirror symmetry conditions. In addition, the complete and extrapolated scattering matrix of cypress pollen has been reported for the first time. Comparison of the backscattering depolarization ratios derived from these matrices indicates that depolarization lidars are not suitable to differentiate these particles in the field, not even if size is the only physical parameter considered. To distinguish these types of aerosol, scattering-angle resolved measurements of additional element of the scattering matrix are required. In particular, we find that the diagonal elements F_{22}/F_{11} and F_{44}/F_{11} are suitable for this task, since they are sensitive to particle structure, which appears to be the only physically relevant difference between volcanic ash and desert dust from the point of view of atmospheric retrieval by light scattering observations. Comparison of the scattering matrices of many different samples compiled in the Granada-Amsterdam database indicates that samples can be classified in two groups depending on their surface structure (smooth-compact or uneven-aggregate). The uneven surfaces of aggregates produce lower values of F_{22}/F_{11} and F_{44}/F_{11} than the smoother surfaces of compact particles across the complete scattering angle range. The vesicles of volcanic ashes appear to play no role in this, since they are generally larger than the effective radii of their size distributions. For cypress pollen, which is virtually monodisperse and presents more regular shapes, the -F_{12}/F_{11} element on its own appears to offer enough contrast against mineral samples, although measurements of the scattering matrix of a wider range of pollen types are required to assess the potential of polarimetry to identify them.

CRediT authorship contribution statement

Juan Carlos Gómez Martín: Conceptualization; Formal analysis; Funding acquisition; Investigation; Methodology; Visualization; Writing - original draft. Daniel Guirado: Methodology; Software; Data curation; Writing – review & editing. Elisa Frattin: Investigation. Maria Bermudez-Edo: Writing – review & editing. Paloma Cariñanos Gonzalez: Resources. Francisco José Olmo Reyes: Resources. Timo Nousiainen: Resources; Writing – review & editing. Pedro J. Gutiérrez: Writing – review & editing. Fernando Moreno: Funding acquisition; Project administration; Methodology; Writing – review & editing. Olga Muñoz: Conceptualization; Funding acquisition; Project administration; Investigation; Methodology; Resources; Writing – review & editing.

Data availability statement

The data generated and used in this research can be freely downloaded from the Granada-Amsterdam online scattering database (https://www.iaa.csic.es/scattering/).

Declaration of Competing Interest

The authors declare that they have no known competing financial interests or personal relationships that could have appeared to influence the work reported in this paper.

Acknowledgements

Supplementary materials

Supplementary material associated with this article can be found, in the online version, at doi:10.1016/j.jqsrt.2021.107761.

References

[1] Boucher O, Randall D, Artaxo P, Bretherton C, Feingold G, Forster P, et al. 3: Clouds and Aerosols Climate Change 2013: The Physical Science Basis. Contribution of Working Group I to the Fifth Assessment Report of the Intergovernmental Panel on Climate Chan. Stocker TF, Qin D, Plattner G-K, Tignor M, Allen SK, Boschung J, et al., editors. Cambridge, United Kingdom and New York, NY, USA: Cambridge University Press; 2013.

[2] Ciais P, Sabine C, Bala G, Bopp L, Brovkin V, Canadell J, et al. 6: Carbon and Other Biogeochemical Cycles AR5 Clim. Chang. 2013 Phys. Sci. Basis. Stocker TF, Qin D, Plattner G-K, Tignor M, Allen SK, Boschung J, et al., editors. Cambridge, U K and New York, NY, USA: Cambridge University Press; 2013.

[3] Yu H, Chin M, Yuan T, Bian H, Remer LA, Prospero JM, et al. The fertilizing role of African dust in the Amazon rainforest: A first multiyear assessment based on data from Cloud-Aerosol Lidar and Infrared Pathfinder Satellite Observations. Geophys Res Lett 2015;42:1984–91. doi:10.1002/2015GL063040.

[4] Kaufman YJ, Koren I, Remer LA, Tanré D, Ginoux P, Fan S. Dust transport and deposition observed from the Terra-Moderate Resolution Imaging Spectroradiometer (MODIS) spacecraft over the Atlantic Ocean. J Geophys Res Atmos 2005;110. doi:10.1029/2003JD004436.

[5] Sassen K. Indirect climate forcing over the western US from Asian dust storms. Geophys Res Lett 2002;29 103-1-103–4. doi:10.1029/2001GL014051.

[6] Zhu Y, Toon OB, Jensen EJ, Bardeen CG, Mills MJ, Tolbert MA, et al. Persisting volcanic ash particles impact stratospheric SO2 lifetime and aerosol optical properties. Nat Commun 2020;11:4526. doi:10.1038/s41467-020-18352-5.

[7] Mather TA, Pyle DM, Oppenheimer C. Tropospheric volcanic aerosol. In: Robock A, Oppenheimer C, (Eds.), Volcanism Earth's Atmos., vol. 139, American Geophysical UnioN; 2004. 10.1029/139GM12.

[8] Prata AJ. Satellite detection of hazardous volcanic clouds and the risk to global air traffic. Nat Hazards 2009;51:303–24.

[9] Després V, Huffman JA, Burrows SM, Hoose C, Safatov A, Buryak G, et al. Primary biological aerosol particles in the atmosphere: a review. Tellus B Chem Phys Meteorol 2012;64:15598. doi:10.3402/tellusb.v64i0.15598.

[10] Andreae MO, Rosenfeld D. Aerosol–cloud–precipitation interactions. Part 1. the nature and sources of cloud-active aerosols. Earth-Science Rev 2008;89:13–41. doi:10.1016/j.earscirev.2008.03.001.

[11] Pöschl U, Martin ST, Sinha B, Chen Q, Gunthe SS, Huffman JA, et al. Rainforest aerosols as biogenic nuclei of clouds and precipitation in the Amazon. Science (80-) 2010;329:1513. doi:10.1126/science.1191056.

[12] Prenni AJ, Petters MD, Kreidenweis SM, Heald CL, Martin ST, Artaxo P, et al. Relative roles of biogenic emissions and Saharan dust as ice nuclei in the Amazon basin. Nat Geosci 2009;2:402–5. doi:10.1038/ngeo517.

[13] Diehn S, Zimmermann B, Tafintseva V, Bağcıoğlu M, Kohler A, Ohlson M, et al. Discrimination of grass pollen of different species by FTIR spectroscopy of individual pollen grains. Anal Bioanal Chem 2020;412:6459–74. doi:10.1007/s00216-020-02628-2.

[14] Frank U, Ernst D. Effects of NO2 and Ozone on Pollen Allergenicity. Front Plant Sci 2016;7. doi:10.3389/fpls.2016.00091.

[15] Querol X, Tobías A, Pérez N, Karanasiou A, Amato F, Stafoggia M, et al. Monitoring the impact of desert dust outbreaks for air quality for health studies. Environ Int 2019;130:104867. doi:10.1016/j.envint.2019.05.061.

[16] Zhang X, Zhao L, Tong DQ, Wu G, Dan M, Teng B. A systematic review of global desert dust and associated human health effects. Atmosphere (Basel) 2016;7:158. doi:10.3390/atmos7120158.

[17] Holben BN, Eck TF, Slutsker I, Tanré D, Buis JP, Setzer A, et al. AERONET—A Federated Instrument Network and Data Archive for Aerosol Characterization. Remote Sens Environ 1998;66:1–16. doi:10.1016/S0034-4257(98)00031-5.

[18] Dubovik O, King MD. A flexible inversion algorithm for retrieval of aerosol optical properties from Sun and sky radiance measurements. J Geophys Res Atmos 2000;105:20673–96. doi:10.1029/2000JD900282.

[19] Dubovik O, Sinyuk A, Lapyonok T, Holben BN, Mishchenko M, Yang P, et al. Application of spheroid models to account for aerosol particle nonsphericity in remote sensing of desert dust. J Geophys Res Atmos 2006;111. doi:10.1029/2005JD006619.

[20] Guirado C, Cuevas E, Cachorro VE, Toledano C, Alonso-Pérez S, Bustos JJ, et al. Aerosol characterization at the Saharan AERONET site Tamanrasset. Atmos Chem Phys 2014;14:11753–73. doi:10.5194/acp-14-11753-2014.

[21] Ansmann A, Tesche M, Seifert P, Groß S, Freudenthaler V, Apituley A, et al. Ash and fine-mode particle mass profiles from EARLINET-AERONET observations over central Europe after the eruptions of the Eyjafjallajökull volcano in 2010. J Geophys Res Atmos 2011;116. doi:10.1029/2010JD015567.

[22] Dubovik O, Li Z, Mishchenko MI, Tanré D, Karol Y, Bojkov B, et al. Polarimetric remote sensing of atmospheric aerosols: Instruments, methodologies, results, and perspectives. vol. 224. 2019. https://doi.org/10.1016/j.jqsrt.2018.11.024.

[23] Ansmann A, Mattis I, Müller D, Wandinger U, Radlach M, Althausen D, et al. Ice formation in Saharan dust over central Europe observed with temperature/humidity/aerosol Raman lidar. J Geophys Res Atmos 2005;110. doi:10.1029/2004JD005000.

[24] Ansmann A, Seifert P, Tesche M, Wandinger U. Profiling of fine and coarse particle mass: case studies of Saharan dust and Eyjafjallajökull/Grimsvötn volcanic plumes. Atmos Chem Phys 2012;12:9399–415. doi:10.5194/acp-12-9399-2012.

[25] Groß S, Freudenthaler V, Schepanski K, Toledano C, Schäfler A, Ansmann A, et al. Optical properties of long-range transported Saharan dust over Barbados as measured by dual-wavelength depolarization Raman lidar measurements. Atmos Chem Phys 2015;15:11067–80. doi:10.5194/acp-15-11067-2015.

[26] Mamouri RE, Ansmann A. Fine and coarse dust separation with polarization lidar. Atmos Meas Tech 2014;7:3717–35. doi:10.5194/amt-7-3717-2014.

[27] Sassen K. The polarization lidar technique for cloud research: a review and current assessment. Bull Am Meteorol Soc 1991;72:1848–66. doi:10.1175/1520-0477(1991)072⟨1848:tpltfc⟩2.0.co;2.

[28] Marenco F, Johnson B, Turnbull K, Newman S, Haywood J, Webster H, et al. Airborne Lidar observations of the 2010 Eyjafjallajökull volcanic ash plume. J Geophys Res Atmos 2011;116. doi:10.1029/2011JD016396.

[29] Sassen K, Zhu J, Webley P, Dean K, Cobb P. Volcanic ash plume identification using polarization lidar: Augustine eruption, Alaska. Geophys Res Lett 2007;34. doi:10.1029/2006GL027237.

[30] Miffre A, Mehri T, Francis M, angle Rairoux PUV–VIS depolarization from Arizona Test Dust particles at exact backscattering. J Quant Spectrosc Radiat Transf 2016;169:79–90. doi:10.1016/j.jqsrt.2015.09.016.

[31] Huffman DR, Swanson BE, Huffman JA. A wavelength-dispersive instrument for characterizing fluorescence and scattering spectra of individual aerosol particles on a substrate. Atmos Meas Tech 2016;9:3987–98. doi:10.5194/amt-9-3987-2016.

[32] Buters JTM, Antunes C, Galveias A, Bergmann KC, Thibaudon M, Galán C, et al. Pollen and spore monitoring in the world. Clin Transl Allergy 2018;8:9. doi:10.1186/s13601-018-0197-8.

[33] Galán C, Smith M, Thibaudon M, Frenguelli G, Oteros J, Gehrig R, et al. Pollen monitoring: minimum requirements and reproducibility of analysis. Aerobiologia (Bologna) 2014;30:385–95. doi:10.1007/s10453-014-9335-5.

[34] Horiuchi R, Yamaguchi T, Hara K. Novel Conductometric sensor for detecting pollen using semiconductor thin-film. 2019 IEEE SENSORS 2019:1–4. doi:10.1109/sensors43011.2019.8956686.

[35] Tsuruzoe K, Hara K. Micro Sensors for Real-time Monitoring of Mold Spores and Pollen, 2015, p. 174–9. doi:10.5220/0005279301740179.

[36] Kaye PH, Stanley WR, Hirst E, Foot E V, Baxter KL, Barrington SJ. Single particle multichannel bio-aerosol fluorescence sensor. Opt Express 2005;13:3583–93. doi:10.1364/opex.13.003583.

[37] Kendjel A, Zimmermann B. Chemical analysis of pollen by FT-Raman and FTIR spectroscopies. Front Plant Sci 2020;11. doi:10.3389/fpls.2020.00352.

[38] Mondol AS, Patel MD, Rüger J, Stiebing C, Kleiber A, Henkel T, et al. Application of High-Throughput Screening Raman Spectroscopy (HTS-RS) for label-free identification and molecular characterization of pollen. Sensors 2019;19:4428. doi:10.3390/s19204428.

[39] Chappuis C, Tummon F, Clot B, Konzelmann T, Calpini B, Crouzy B. Automatic pollen monitoring: first insights from hourly data. Aerobiologia (Bologna) 2020;36:159–70. doi:10.1007/s10453-019-09619-6.

[40] Crouzy B, Stella M, Konzelmann T, Calpini B, Clot B. All-optical automatic pollen identification: towards an operational system. Atmos Environ 2016;140:202–12. doi:10.1016/j.atmosenv.2016.05.062.

[41] Hernandez M, Perring AE, McCabe K, Kok G, Granger G, Baumgardner D. Chamber catalogues of optical and fluorescent signatures distinguish bioaerosol classes. Atmos Meas Tech 2016;9:3283–92. doi:10.5194/amt-9-3283-2016.

[42] Kiselev D, Bonacina L, Wolf J-P. Individual bioaerosol particle discrimination by multi-photon excited fluorescence. Opt Express 2011;19:24516–21. doi:10.1364/oe.19.024516.

[43] O'Connor DJ, Healy DA, Hellebust S, Buters JTM, Sodeau JR. Using the WIBS-4 (Waveband Integrated Bioaerosol Sensor) technique for the on-line detection of pollen grains. Aerosol Sci Technol 2014;48:341–9. doi:10.1080/02786826.2013.872768.

[44] Perring AE, Schwarz JP, Baumgardner D, Hernandez MT, Spracklen D V, Heald CL, et al. Airborne observations of regional variation in fluorescent aerosol across the United States. J Geophys Res Atmos 2015;120:1153–70. doi:10.1002/2014JD022495.

[45] Ruske S, Topping DO, Foot VE, Morse AP, Gallagher MW. Machine learning for improved data analysis of biological aerosol using the WIBS. Atmos Meas Tech 2018;11:6203–30. doi:10.5194/amt-11-6203-2018.

[46] Šaulienė I, Šukienė L, Daunys G, Valiulis G, Vaitkevičius L, Matavulj P, et al. Automatic pollen recognition with the Rapid-E particle counter: the first-level procedure, experience and next steps. Atmos Meas Tech 2019;12:3435–52. doi:10.5194/amt-12-3435-2019.

[47] Savage NJ, Huffman JA. Evaluation of a hierarchical agglomerative clustering method applied to WIBS laboratory data for improved discrimination of biological particles by comparing data preparation techniques. Atmos Meas Tech 2018;11:4929–42. doi:10.5194/amt-11-4929-2018.

[48] Sauvageat E, Zeder Y, Auderset K, Calpini B, Clot B, Crouzy B, et al. Real-time pollen monitoring using digital holography. Atmos Meas Tech 2020;13:1539–50. doi:10.5194/amt-13-1539-2020.

[49] Oteros J, Buters J, Laven G, Röseler S, Wachter R, Schmidt-Weber C, et al. Errors in determining the flow rate of Hirst-type pollen traps. Aerobiologia (Bologna) 2017;33:201–10. doi:10.1007/s10453-016-9467-x.

[50] Oteros J, Pusch G, Weichenmeier I, Heimann U, Möller R, Röseler S, et al. Automatic and online pollen monitoring. Int Arch Allergy Immunol 2015;167:158–66. doi:10.1159/000436968.

[51] Cao N, Saukh O, Thiele L. Poster abstract: an automated real-time and affordable airborne pollen sensing system. In: 2019 18th ACM/IEEE Int. Conf. Inf. Process. Sens. Networks; 2019. p. 321–2.

[52] Kawashima S, Clot B, Fujita T, Takahashi Y, Nakamura K. An algorithm and a device for counting airborne pollen automatically using laser optics. Atmos Environ 2007;41:7987–93. doi:10.1016/j.atmosenv.2007.09.019.

[53] Kawashima S, Thibaudon M, Matsuda S, Fujita T, Lemonis N, Clot B, et al. Automated pollen monitoring system using laser optics for observing seasonal changes in the concentration of total airborne pollen. Aerobiologia (Bologna) 2017;33:351–62. doi:10.1007/s10453-017-9474-6.

[54] Berg MJ, Videen G. Digital holographic imaging of aerosol particles in flight. J Quant Spectrosc Radiat Transf 2011;112:1776–83. doi:10.1016/j.jqsrt.2011.01.013.

[55] Kemppinen O, Laning JC, Mersmann RD, Videen G, Berg MJ. Imaging atmospheric aerosol particles from a UAV with digital holography. Sci Rep 2020;10:16085. doi:10.1038/s41598-020-72411-x.

[56] Iwai T. Polarization analysis of light scattered by pollen grains of Cryptomeria Japonica. Jpn J Appl Phys 2013;52:62404. doi:10.7567/jjap.52.062404.

[57] Saito Y, Ichihara K, Morishita K, Uchiyama K, Kobayashi F, Tomida T. Remote detection of the fluorescence spectrum of natural pollens floating in the atmosphere using a Laser-Induced-Fluorescence Spectrum (LIFS) Lidar. Remote Sens 2018;10:1533.

[58] Sassen K. Boreal tree pollen sensed by polarization lidar: Depolarizing biogenic chaff. Geophys Res Lett 2008;35. doi:10.1029/2008gl035085.

[59] Muñoz O, Moreno F, Guirado D, Ramos JL, López A, Girela F, et al. Experimental determination of scattering matrices of dust particles at visible wavelengths: the IAA light scattering apparatus. J Quant Spectrosc Radiat Transf 2010;111:187–96. doi:10.1016/j.jqsrt.2009.06.011.

[60] Muñoz O, Moreno F, Guirado D, Dabrowska DD, Volten H, Hovenier JW. The Amsterdam-Granada Light Scattering Database. J Quant Spectrosc Radiat Transf 2012;113:565–74. doi:10.1016/j.jqsrt.2012.01.014.

[61] Järvinen E, Kemppinen O, Nousiainen T, Kociok T, Möhler O, Leisner T, et al. Laboratory investigations of mineral dust near-backscattering depolarization ratios. J Quant Spectrosc Radiat Transf 2016;178:192–208. doi:10.1016/j.jqsrt.2016.02.003.

[62] Muñoz O, Moreno F, Guirado D, Ramos JL, Volten H, Hovenier JW. The IAA cosmic dust laboratory: experimental scattering matrices of clay particles. Icarus 2011;211:894–900. doi:10.1016/j.icarus.2010.10.027.

[63] Hovenier JW. Measuring scattering matrices of small particles at optical wavelengths. Light Scatt. by nonspheerical Part. Theory, Meas. Appl., Mishchenko MI, Hovenier JW, Travis LD, editors. San Diego, CA, USA: Academic Press; 2000.

[64] Mishchenko MI, Travis LD, Lacis AA. Scattering, absorption and emission of light by small particles. Cambridge, UK: Cambridge University Press; 2002.

[65] Hovenier JW, Van Der Mee C, Domke H. Transfer of Polarized Light in Planetary Atmospheres: Basic Concepts and Practical Methods, 318. Dordrecht, NE: Kluwer; 2004.

[66] Mishchenko MI, Hovenier JW. Depolarization of light backscattered by randomly oriented nonspherical particles. Opt Lett 1995;20:1356–8. doi:10.1364/ol.20.001356.

[67] Moreno F. A Monte Carlo code to compute energy fluxes in Cometary Nuclei. Icarus 2002;156:474–84. doi:10.1006/icar.2001.6806.

[68] Escobar-Cerezo J, Muñoz O, Moreno F, Guirado D, Gómez Martín JC, Goguen JD, et al. An experimental scattering matrix for lunar regolith simulant JSC-1A at visible wavelengths. Astrophys J Suppl Ser 2018;235:19. doi:10.3847/1538-4365/aaa6cc.

[69] van de Hulst HC. Light scattering by small particles. Courier 1981.

[70] Mishchenko MI. Electromagnetic scattering by nonspherical particles: a tutorial review. J Quant Spectrosc Radiat Transf 2009;110:808–32. doi:10.1016/j.jqsrt.2008.12.005.

[71] Hovenier JW, Guirado D. Zero slopes of the scattering function and scattering matrix for strict forward and backward scattering by mirror symmetric collections of randomly oriented particles. J Quant Spectrosc Radiat Transf 2014;133:596–602. doi:10.1016/j.jqsrt.2013.09.023.

[72] Miffre A, Cholleton D, Rairoux P. Laboratory evaluation of the scattering matrix elements of mineral dust particles from 176.0° up to 180.0°-exact backscattering angle. J Quant Spectrosc Radiat Transf 2019;222–223:45–59. doi:10.1016/j.jqsrt.2018.10.019.

[73] Volten H, Muñoz O, Rol E, de Haan JF, Vassen W, Hovenier JW, et al. Scattering matrices of mineral aerosol particles at 441.6 nm and 632.8 nm. J Geophys Res Atmos 2001;106:17375–401. doi:10.1029/2001jd900068.

[74] Muñoz O, Volten H, de Haan JF, Vassen W, Hovenier JW. Experimental determination of the phase function and degree of linear polarization of El Chichón and Pinatubo volcanic ashes. J Geophys Res Atmos 2002;107 ACL 4-1-ACL 4-8. doi:10.1029/2001jd000983.

[75] Muñoz O, Volten H, Hovenier JW, Veihelmann B, van der Zande WJ, Waters LBFM, et al. Scattering matrices of volcanic ash particles of Mount St. Helens, Redoubt, and Mount Spurr Volcanoes. J Geophys Res Atmos 2004;109:D16201. doi:10.1029/2004jd004684.

[76] Merikallio S, Muñoz O, Sundström A-M, Virtanen TH, Horttanainen M, de Leeuw G, et al. Optical modeling of volcanic ash particles using ellipsoids. J Geophys Res Atmos 2015;120:4102–16. doi:10.1002/2014jd022792.

[77] Hansen JE, Travis LD. Light scattering in planetary atmospheres. Space Sci Rev 1974;16:527–610. doi:10.1007/BF00168069.

[78] Cariñanos P, Adinolfi C, Díaz de la Guardia C, De Linares C, Casares-Porcel M. Characterization of allergen emission sources in urban areas. J Environ Qual 2016;45:244–52. doi:10.2134/jeq2015.02.0075.

[79] Díaz de la Guardia C, Alba F, de Linares C, Nieto-Lugilde D, López Caballero J. Aerobiological and allergenic analysis of Cupressaceae pollen in Granada (Southern Spain). J Investig Allergol Clin Immunol 2006;16:24–33.

[80] Cariñanos P, Foyo-Moreno I, Alados I, Guerrero-Rascado JL, Ruiz-Peñuela S, Titos G, et al. Bioaerosols in urban environments: Trends and interactions with pollutants and meteorological variables based on quasi-climatological series. J Environ Manage 2021;282:111963. doi:10.1016/j.jenvman.2021.111963.

[81] Ebert M, Weinbruch S, Rausch A, Gorzawski G, Helas G, Hoffmann P, et al. Complex refractive index of aerosols during LACE 98#x2010; as derived from the analysis of individual particles. J Geophys Res Atmos 2002;107 LAC 3-1-LAC 3-15. doi:10.1029/2000jd000195.

[82] Kim G, Lee S, Shin S, Park Y. Three-dimensional label-free imaging and analysis of Pinus pollen grains using optical diffraction tomography. Sci Rep 2018;8:1782. doi:10.1038/s41598-018-20113-w.

[83] Gómez Martín JC, Guirado D, Zubko E, Escobar-Cerezo J, Moreno F, Muñoz O. Computational study of the sensitivity of laser light scattering particle sizing to refractive index and irregularity. J Quant Spectrosc Radiat Transf 2020;241:106745. doi:10.1016/j.jqsrt.2019.106745.

[84] Proussevitch AA, Mulukutla GK, Sahagian DL. A new 3D method of measuring bubble size distributions from vesicle fragments preserved on surfaces of volcanic ash particles. Geosphere 2011;7:62–9. doi:10.1130/GES00559.1.

[85] Bortennschlager S. Aspects of pollen morphology in the Cupressaceae. Grana 1990;29:129–38.

[86] Macke A, Mishchenko MI, Muinonen K, Carlson BE. Scattering of light by large nonspherical particles: ray-tracing approximation versus T-matrix method. Opt Lett 1995;20:1934. doi:10.1364/ol.20.001934.

[87] Parviainen P, Bohren CF, Mäkelä V. Vertical elliptical coronas caused by pollen. Appl Opt 1994;33:4548. doi:10.1364/ao.33.004548.

[88] Tränkle E, Mielke B. Simulation and analysis of pollen coronas. Appl Opt 1994;33:4552. doi:10.1364/ao.33.004552.

[89] Sorensen C, Heinson Y, Heinson W, Maughan J, Chakrabarti A. Q-Space analysis of the light scattering phase function of particles with any shape. Atmosphere (Basel) 2017;8:68. doi:10.3390/atmos8040068.

[90] Sakai T, Nagai T, Zaizen Y, Mano Y. Backscattering linear depolarization ratio measurements of mineral, sea-salt, and ammonium sulfate particles simulated in a laboratory chamber. Appl Opt 2010;49:4441–9. doi:10.1364/AO.49.004441.

[91] Bohlmann S, Shang X, Giannakaki E, Filioglou M, Saarto A, Romakkaniemi S, et al. Detection and characterization of birch pollen in the atmosphere using a multiwavelength Raman polarization lidar and Hirst-type pollen sampler in Finland. Atmos Chem Phys 2019;19:14559–69. doi:10.5194/acp-19-14559-2019.

[92] Sassen K. Polarization in Lidar. Lidar. Springer-Verlag 2006:19–42. doi:10.1007/0-387-25101-4_2.

[93] Kahnert M, Kanngießer F, Järvinen E, Schnaiter M. Aerosol-optics model for the backscatter depolarisation ratio of mineral dust particles. J Quant Spectrosc Radiat Transf 2020;254:107177. doi:10.1016/j.jqsrt.2020.107177.

[94] Roy G, Tremblay G, Cao X. Scattering phase function depolarization parameter model and its application to water droplets sizing using off-axis lidar measurements at multiple angles. Appl Opt 2018;57:969. doi:10.1364/ao.57.000969.

[95] Tremblay G, Roy G, Bernier R, Cao X. Experimental validation of D parameter model for droplet sizing using off-axis lidar measurements. Appl Opt 2019;58:6949. doi:10.1364/ao.58.006949.

[96] Cholleton D, Bialic E, Dumas A, Kaluzny P, Rairoux P, Miffre A. Laboratory evaluation of the (VIS, IR) scattering matrix of complex-shaped ragweed pollen particles. J Quant Spectrosc Radiat Transf 2020;254:107223. doi:10.1016/j.jqsrt.2020.107223.

[97] Cao X, Roy G, Bernier R. Lidar polarization discrimination of bioaerosols. Opt Eng 2010;49:116201.

[98] Piedra P, Gobert C, Kalume A, Le Pan Y, Kocifaj M, Muinonen K, et al. Where is the machine looking? locating discriminative light-scattering features by class-activation mapping. J Quant Spectrosc Radiat Transf 2020;247:106936. doi:10.1016/j.jqsrt.2020.106936.

[99] OriginLab. Online help: 17.7.3.3 Algorithms (Hierarchical Cluster Analysis) n.d. https://www.originlab.com/doc/Origin-Help/HCA-Algorithm (accessed 23 March 2021).

[100] Mathworks. Online help: Hierarchical Clustering n.d; 2021. https://uk.mathworks.com/help/stats/hierarchical-clustering.html (accessed 23 March).

[101] Hastie T, Tibshirani R, Friedman J. The Elements of Statistical Learning. New York, NY: Springer New York; 2009. doi:101007/978-0-387-84858-7.

[102] Piedra P, Kalume A, Zubko E, Mackowski D, Le Pan Y, Videen G. Particle-shape classification using light scattering: An exercise in deep learning. J Quant Spectrosc Radiat Transf 2019;231:140–56. doi:10.1016/j.jqsrt.2019.04.013.

[103] Lindqvist H, Nousiainen T, Zubko E, Muñoz O. Optical modeling of vesicular volcanic ash particles. J Quant Spectrosc Radiat Transf 2011;112:1871–80. doi:10.1016/j.jqsrt.2011.01.032.

[104] Liu C, Yin Y. Inherent optical properties of pollen particles: a case study for the morning glory pollen. Opt Express 2016;24:A104. doi:10.1364/oe.24.00a104.

[105] Nousiainen T, Kahnert M, Lindqvist H. Can particle shape information be retrieved from light-scattering observations using spheroidal model particles? J Quant Spectrosc Radiat Transf 2011;112:2213–25. doi:10.1016/j.jqsrt.2011.05.008.

[106] Kahnert M, Nousiainen T, Lindqvist H. Review: model particles in atmospheric optics. J Quant Spectrosc Radiat Transf 2014;146:41–58. doi:10.1016/j.jqsrt.2014.02.014.